Fractional Topology in Hybrid Magnetic Skyrmions

by

William S. Parker

A dissertation accepted and approved in partial fulfillment of the
requirements for the degree of
Doctor of Philosophy
in Physics

Dissertation Committee:
Benjamín Alemán, Chair
Benjamin McMorran, Advisor
Tien-Tien Yu, Core Member
Julia Widom, Institutional Representative

University of Oregon
Fall 2024

DISSERTATION ABSTRACT

William S. Parker

Doctor of Philosophy in Physics

Title: Fractional Topology in Hybrid Magnetic Skyrmions

Magnetic materials were first used to record information over a century ago when Valdemar Poulsen used a magnetic wire recorder to record and play back audio in 1900 [1]. From that first device to the magnetic hard drives ubiquitous in big data centers today, there have been seemingly endless schemes for how to use magnetism to store and manipulate information. In that time, semiconductor information storage has gained dominance in consumer devices, but the relatively low cost and long lifespan of hard drives makes them the preferred choice in big data and commercial applications. However, hard drives have their own drawbacks, most notably their energy consumption - a 2016 study estimated that in 2014, U.S. data centers consumed 1.8% of total U.S. power consumption [2]. A more recent study from the Electric Power Research Institute puts that figure at 4% of total U.S. power consumption in 2023, with generative artificial intelligence models pushing that number higher in years to come [3]. The need for low-cost, low-energy, long-lifespan non-volatile computer memory is high and increasing. With this need comes a new candidate information carrier, the magnetic skyrmion. Magnetic skyrmions are topologically protected particle-like magnetic configurations that can be driven through a material at low current densities, making them promising for use in magnetic logic and memory devices. However, their integration into real world devices requires a better understanding of their structure and behavior, and the measurement techniques to achieve that. In this work, I lay out a theoretical framework to capture

the novel topology of skyrmions in one of the most promising host systems, Fe/Gd multilayer thin films, and show how it explains their stability. I then describe novel magnetic imaging techniques, and apply them to this host system to gain a full understanding of the skyrmions within it.

This dissertation includes previously published and unpublished co-authored material.

CURRICULUM VITAE

NAME OF AUTHOR: William S. Parker

GRADUATE AND UNDERGRADUATE SCHOOLS ATTENDED:

University of Oregon, Eugene, OR, USA
Chapman University, Orange, CA, USA

DEGREES AWARDED:

Doctor of Philosophy, Physics, Fall 2024, University of Oregon
Bachelor of Science, Physics, Spring 2018, Chapman University
Bachelor of Science, Mathematics, Spring 2018, Chapman University

AREAS OF SPECIAL INTEREST:

Computational Physics
Electron Microscopy
Magnetic Memory and Logic Devices

PROFESSIONAL EXPERIENCE:

Graduate Research Assistant, University of Oregon, Summer 2018 - Fall 2024
Undergraduate Researcher, Chapman University, Spring 2017 - Spring 2018
Undergraduate Researcher (REU), University of Rochester, Summer 2017

GRANTS, AWARDS AND HONORS:

Best Student Presentation Finalist - Magnetism & Magnetic Materials, Oct 2023
Honorable Mention - NSF GRFP, Apr 2020
Graduate First Year Fellowship - University of Oregon, Fall 2018 - Spring 2019
OMQ Director's Fellowship - University of Oregon, Fall 2018

PUBLICATIONS:

Parker, W. S., Montoya, S. A., Fullerton, E. E., McMorran, B. J. Combining Lorentz TEM and SEM with Polarization Analysis to Uncover Fractional Topological Spin Textures in Fe/Gd Multilayer Thin Films. *Microscopy and Microanalysis* 2024, 30 (Supplement 1), ozae044.507.

Ducharme, A., Parker, W., Yasin, F. S., Yu, X., McMorran, B. Lorentz Scanning Transmission Electron Microscopy Holography (LSTEMH) Measurement of Domain Walls in Fe/Gd Multilayers. *Microscopy and Microanalysis* 2024, 30 (Supplement 1), ozae044.510.

Parker, W. S., Montoya, S. A., Fullerton, E. E., McMorran, B. J. Evolution of Novel Chiral Spin Textures in Fe/Gd Based Multilayer Thin Films. *Microscopy and Microanalysis* 2022, 28 (S1), 2336-2337.

Reddinger, J., Parker, W. Micromagnetics Simulation as a Supplement to and Diagnostic for Lorentz Transmission Electron Microscopy. *Microscopy and Microanalysis* 2022, 28 (S1), 1694-1696.

Parker, W., Montoya, S., Fullerton, E., McMorran, B. Chiral Spin Textures in Fe/Gd Based Multilayer Thin Films. *Microsc Microanal* 2021, 27 (S1), 2404-2407.

Johnson, C. W., Pierce, J. S., Moraski, R. C., Turner, A. E., Greenberg, A. T., Parker, W. S., McMorran, B. J. Exact Design of Complex Amplitude Holograms for Producing Arbitrary Scalar Fields. *Opt. Express* 2020, 28 (12), 17334.

Parker, W., McMorran, B. Feasibility of an Electron Orbital Angular Momentum Sorter. *Microsc Microanal* 2019, 25 (S2), 90-91.

TABLE OF CONTENTS

Chapter Page

Chapter Page

LIST OF FIGURES

Figure Page

LIST OF TABLES

Table Page

CHAPTER I

INTRODUCTION

1.1 A Brief History of Magnetic Recording

At the Paris Exposition of 1900, Valdemar Poulsen demonstrated a device called a telegraphone that used a magnetic wire coiled around a drum to record and play back audio. Audio was translated to a varying electrical signal, which in turn was fed to a recording head which induced a varying magnetization pattern in the magnetic wire. The playback head worked in reverse, with the varying magnetization inducing an electrical signal to be fed into a speaker [1]. This device precursed the magnetic tape recorder and was the first demonstration of a magnetic recording device.

In the century following, innumerable configurations have been developed that use magnetization to store information. Some, like magnetic tape, store effectively analog data, while others like the modern hard drive store binary data in discrete magnetic domains. Different technologies found niches in the market throughout the years, especially as either storage or random-access memory (RAM) for computers. Core rope memory, a read-only technology, found use in the Apollo missions [4]. Magnetic-core memory dominated computer RAM until the mid 1970s, when semiconductor memory surpassed it in cost and ease of manufacturing, in particular dynamic RAM (DRAM) [5]. The configuration of most magnetic recording technologies is essentially the same as the telegraphone that began the field: a magnetic medium whose magnetization stores the information, and a read-write head to change and measure its magnetization. The read-write head moves to the relevant position on the tape, reads or writes information, and moves on.

A development called bubble memory presented a fundamentally different paradigm, in which both the recording medium and the read-write head are stationary,

and the magnetic configuration itself moves through the material, pushed by an electrical current [6]. The potential benefits of this setup are huge: with no moving parts, the energy efficiency increases and the points of failure decrease. At its initial inception, it held immense promise as the memory device of the future, but the rapid improvements made to hard drive and semiconductor memory prevented their widespread adoption. However, the idea of current-driven magnetic memory has had a resurgence in recent years due to advances in current-driven domain wall motion [7] and proposals for racetrack memory devices using magnetic skyrmions [8].

Skyrmions are topologically protected field configurations, originally proposed to model the nucleon by Tony Skyrme [9, 10]. In magnetic materials, the magnetization can be treated as a continuous vector field, and the magnetic skyrmion as a two-dimensional particle-like topological soliton in this vector field. Observation of magnetic skyrmions came first via neutron scattering in 2009 by Mühlbauer *et al.* [11] and soon after by Lorentz transmission electron microscopy (LTEM) by Yu *et al.* [12]. Real interest was generated two years later when Yu *et al.* used LTEM to capture skyrmion motion driven by ultra-low current densities [13]. These low current densities, topological stability, and particle-like nature position the skyrmion as an extremely appealing information carrier in spintronic logic and memory devices.

1.2 Topological Solitons in 2D and in 3D

In magnetic systems, the magnetization is treated as a spatially dependent, continuous vector field $\mathbf{m}(x, y, z)$ with unit modulus $|\mathbf{m}| = 1$. Static solutions are found by minimizing the energy of the system, which itself is a function of the spatially dependent magnetization and any external fields. Dynamics are given by the Landau-Lifshitz-Gilbert (LLG) equation of motion, which describes damped precession based on the effective field. Analytical solutions are relatively rare, so

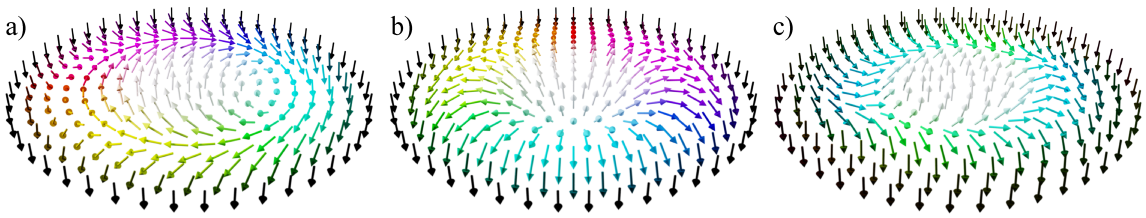

Figure 1. Schematic of (a) a Bloch-type skyrmion, (b) a Néel-type skyrmion, and (c) a trivial bubble. They are all characterized by a central magnetic domain where $m_z > 0$, surrounded by a region where $m_z < 0$. In (a) and (b), the domain wall wraps continuously around the center, which prevents smooth transformations to the uniform state.

the use of micromagnetic simulations is common, and commercial software has been developed to make micromagnetics simulations straightforward and standardized [14].

Static solutions often take the form of magnetic domains, isolated regions in which the magnetization is uniform. Domains are separated by transition regions called domain walls (DWs). Many systems have an axis along which magnetization prefers to align called an easy axis. In the multilayer thin films discussed in this dissertation, the easy axis is normal to the plane of the thin film, resulting in magnetic domains oriented into or out of the plane, and domain walls lying in-plane.

Magnetic skyrmions are particle-like configurations of the magnetization. They take the form of isolated, circular magnetic domains, with domain walls wrapped smoothly around them, as shown in Fig. 1 (a) and (b). This continuous wrapping is integral to the skyrmion's stability, as it prevents the isolated domain from aligning with its surrounding region. In contrast, Fig. 1 (c) shows a trivial bubble - an isolated domain whose domain wall does not wrap continuously around it. As a result, the trivial bubble is not truly isolated from the surrounding region, and could be smoothly transformed into a uniform magnetization.

The lack of smooth transformation between states is captured by topological classification of the states. In the simplest sense, the solutions to a physical system

- i.e., the configurations of the magnetization - may be divided into distinct classes, which cannot be continuously transformed into one another. This concept often comes with localization, as the behavior at the edge of a system is often what prevents these continuous transformations. Magnetic skyrmions are an example of a topological soliton; a localized configuration with no continuous transformation to the uniform state.

Magnetic skyrmions are characterized by a non-zero topological number, or skyrmion number, N_{sk}, defined as

$$N_{sk} = \frac{1}{4\pi} \int \mathbf{m} \cdot [\partial_x \mathbf{m} \times \partial_y \mathbf{m}] \, \mathrm{d}x\mathrm{d}y. \tag{1.1}$$

Formally, this integer-valued index divides the solutions for $\mathbf{m}$ into homotopy classes. Magnetic skyrmions have skyrmion number $N_{sk} = 1$, while the trivial bubble in Fig. 1 (c) has skyrmion number $N_{sk} = 0$ - the same as a uniform magnetization. In reality, the magnetization is not truly continuous (being instead defined for each atom in the material) and this division physically translates to a large energy barrier associated with the annihilation of a skyrmion. Note that geometrically distinguishable textures may belong to the same homotopy class; for example, Fig. 1 (a) and (b) show two types of skyrmions, each with $N_{sk} = 1$. Transformations between the two types - called Bloch and Néel skyrmions - are smooth, but the removal of the central domain, transforming to a uniform magnetization, is discontinuous.

The skyrmion number N_{sk} is a 2D characterization, but most real magnetic systems exist in 3D. In many systems, like thin films and bulk crystals, the skyrmion is assumed to be uniform through the thickness. However, this is not always an accurate picture. The skyrmion may vary geometrically through the thickness - for example, since smooth transformations between Néel and Bloch skyrmions are allowed, the magnetization might be Bloch-type at one z value, but twist to Néel-type at another.

The idea of topological number extends to three dimensions via the Hopf index

$$H = -\frac{1}{(8\pi)^2}\int \mathbf{F}\cdot\mathbf{A}\mathrm{d}^3\mathbf{r} \tag{1.2}$$

where $\mathbf{F}$ is the emergent magnetic field and $\mathbf{A}$ its vector potential [15]. This extends the idea of magnetic solitons to three dimensions, and captures both their stability and localization in the same way that the skyrmion number does for 2D configurations.

1.3 Skyrmions in Multilayer Thin Films

Magnetic skyrmions were first observed in non-centrosymmetric crystals [11], whose lack of inversion symmetry leads to a non-zero, non-collinear Dzyaloshinskii-Moriya Interaction (DMI) [16, 12, 17]. Competing against collinear energetics terms, the DMI leads to a canting between pairs of spins, and thus stabilizes skyrmions and other chiral textures whose handedness and geometric properties are tied to the crystalline structure.

To facilitate skyrmions' use in real world applications, however, recent research has focused on multilayer thin films, which can be tuned to host skyrmions at ambient conditions, i.e., at room temperature and with no applied field [18, 19, 20, 21, 22]. Skyrmions in these systems form as a result of competing dipolar and exchange interactions, without the need for DMI, which also means skyrmions of opposite handedness can exist simultaneously. Recent work has shown that the surface-volume stray field interactions in these films have the form of a layer-dependent interfacial DMI [22, 23]. As a result, they are expected to have a hybrid structure, consisting of a naturally Bloch-type DW in the center of the film which twists toward Néel-type at the surfaces to align with the stray dipolar fields from the out-of-plane core of the skyrmion, shown in Fig. 2. This alignment naturally results in Néel caps with opposite helicities, and thus the helicity of a hybrid skyrmion varies monotonically from one surface to the opposite.

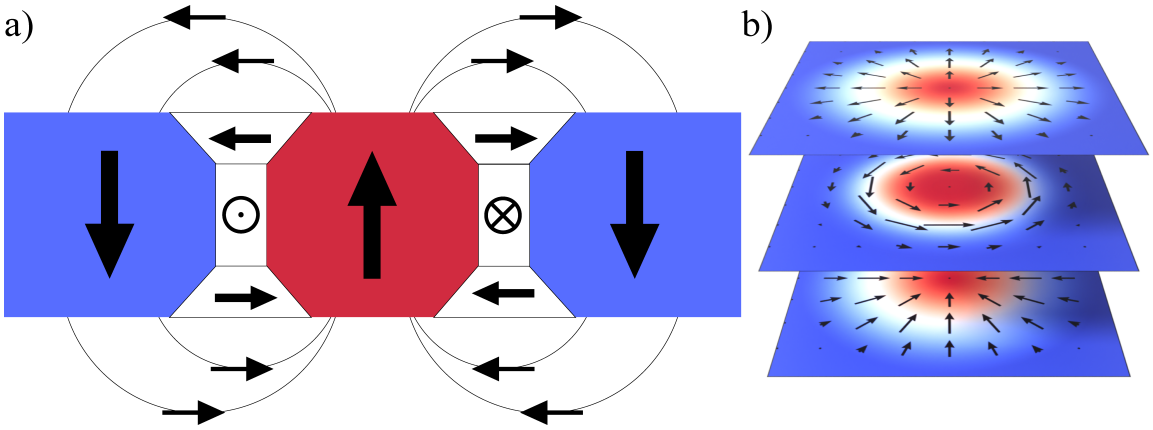

Figure 2. Schematic representation of a hybrid skyrmion's structure. (a) The cross-section of the skyrmion, with the isolated core in red and the surrounding region in blue. The top and bottom of the DWs twist to align with the dipolar stray field, resulting in (b) a skyrmion with a Bloch core and Néel caps of opposite helicities.

These Néel caps, which are a general feature of skyrmions in multilayer thin films [22], play a vital role in the behavior of the skyrmion. They act as flux closure domains, bringing stray field lines into the material and thus lowering the energetic cost of the skyrmion. This, along with their tunability, is why multilayer thin films can host such stable skyrmions even at room temperature and without a stabilizing applied field. At the same time, the helicity of a skyrmion affects its response to applied currents, so understanding the structure and dynamics of hybrid skyrmions is critical for progressing toward real-world applications. One of the key findings of this work is that the 3D variation in helicity creates 3D topological structure distinct from that of a skyrmion which is uniform through the thickness.

1.4 Characterization of Magnetic Textures

A number of techniques exist for the characterization of magnetic textures, each with its own limitations. They fall into two main categories: projective techniques and surface-sensitive techniques. Projective techniques transmit light or particles through the sample, and any signal acquired is therefore integrated through its

thickness. Surface-sensitive techniques either reflect particles or light off the surface, or measure light or electrons ejected from the surface. Imaging techniques can further be classified by the type of particle or light used - with electrons, neutrons, and X-rays the most common - which determines the information accessed as well as the resolution available.

The transmission electron microscope (TEM) is one of the most common platforms for magnetic imaging. It can operate in two fundamental modes: transmission electron microscopy, in which the sample is illuminated by a plane wave of electrons, and scanning transmission electron microscopy (STEM), in which a focused electron probe is rastered across the sample in a grid pattern to form an image pixel-by-pixel. Both modes are projective. Since fast electrons have an extremely small wavelength, on the order of picometers, the available resolution is excellent. They are deflected by magnetic fields perpendicular to their motion, so TEM and STEM magnetic imaging access the transverse magnetic induction; that is, $\mathbf{B}_{xy}$ integrated through z. This can also be formulated in terms of the Aharonov-Bohm phase - the phase acquired by an electron passing through a magnetic vector potential - which is useful for analysis as it translates the reconstruction problem from ray optics to Fourier optics.

LTEM is one of the most common TEM-based magnetic imaging techniques. However, since it uses plane wave illumination and the magnetic signal is phase-only, it requires defocus to form contrast, which reduces the practical resolution. Differential phase contrast (DPC), a STEM-based technique, measures the deflection of a focused probe at each pixel, and therefore requires no defocus. However, both techniques measure the change in phase from point to point, rather than the absolute phase, which introduces error to the analysis. In addition, they both measure the

magnetic induction, rather than the magnetization itself, and since the induction is integrated through z, a direct connection between the two is difficult to quantitatively establish.

Resonant X-ray techniques are a common alternative to the TEM. They depend on spin-dependent atomic absorption, so they are sensitive to m_z, integrated through z. However, the resolution is rarely good enough to measure relevant phenomena, and so reciprocal-space imaging is common. Both projective and reflective neutron techniques are also common, but resolution is again limited. Therefore reciprocal-space measurements are common in projective neutron techniques. One advantage to reflective neutron techniques is that depth-dependent phenomena can be captured by varying the reflection angle, but no xy-dependent resolution is retained. The closest technique to full characterization is Lorentz vector field tomography, but this requires many tilted images to be taken and aligned, and suffers from reconstruction artifacts.

1.5 Outline

The focus of this dissertation is on measuring the 3D structure of magnetic skyrmions and characterizing their topology as 3D solitons. In particular, surface-sensitive scanning electron microscopy with polarization analysis (SEMPA) is combined with projective Lorentz TEM to determine the 3D structure of hybrid magnetic skyrmions in multilayer thin films. STEM holography, an interferometric electron technique which can directly measure point-by-point phase, is used to measure magnetic domains. The advantages presented by STEM holography provide a possible avenue toward improved magnetic vector field tomography [24]. Finally, the 3D structure of magnetic skyrmions in multilayer thin films is shown to introduce non-trivial topology in three dimensions, and this non-triviality is quantitatively related to stability and to surface-sensitive, single-image measurements.

This dissertation is composed primarily of three manuscripts in preparation, for all of which I am the primary author. Additional work from a published conference abstract is included in Chapter V, as is unpublished work completed in collaboration with Sergio Montoya and Eric Fullerton. These chapters are organized as follows: a description of the novel topology of hybrid skyrmions found in magnetic multilayer thin films, real-space characterization of this 3D structure using a combination of SEMPA, LTEM, and micromagnetic simulations, a demonstration of inducing domain wall chirality preference by the inclusion of symmetry-breaking heavy metal layers into Fe/Gd thin films, a resolution to a debate over the spin textures initially reported as skyrmion bound pairs, achieved by tracking their evolution from striped domain walls, a demonstration of STEM holography applied to magnetic samples, and a proposal for dichroism measurements in the electron microscope using electron vortex beams.

The following manuscripts are included in this work:

Chapter II. Hybrid Skyrmions in Magnetic Multilayer Thin Films are Half-Integer Hopfions

William S. Parker, Jacques A. Reddinger, Benjamin J. McMorran. "Hybrid Skyrmions in Magnetic Multilayer Thin Films are Half-Integer Hopfions." Manuscript in Preparation.

The skyrmions found in multilayer thin films have additional three-dimensional structure, with their domain wall helicities twisting through the thickness of the film to create a hybrid skyrmion composed of a Bloch-type core with Néel-type caps of opposite chiralities at the surfaces. In this work, we show that this three-dimensional variation creates additional knotted topological structure, providing an explanation for their exceptional stability in ambient conditions. We show that hybrid skyrmions can be described as half-integer Hopfions, and that their field lines have the knotted

structure of the Hopf fibration. Furthermore, we show that the topological charge of partially twisted hybrid skyrmions can be related to the domain wall helicity at the surfaces, providing a straightforward way to connect experimental measurements to underlying topology.

Chapter III. Real Space Imaging of Hybrid Skyrmion Textures in Magnetic Multilayer Thin Films

William S. Parker, Jacques A. Reddinger, Sergio A. Montoya, Eric E. Fullerton, Benjamin J. McMorran. "Real space imaging of hybrid skyrmion textures in magnetic multilayer thin films." Manuscript in Preparation.

The thickness-dependent helicity of hybrid skyrmions underpins their exceptional stability and is predicted to strongly affect their response to driving current and underlying topology. In this paper, we combine LTEM and SEMPA to characterize in real space the 3D structure of hybrid skyrmions. We compare our measurements against micromagnetic simulations, which reveal the full hybrid structure, including the depth dependence of core diameter, domain wall width, and skyrmion helicity.

Chapter V. Tracking the Evolution of Biskyrmion Textures from Domain Wall Stripes

William S. Parker, Sergio A. Montoya, Eric E. Fullerton, Benjamin J. McMorran. "Evolution of Novel Chiral Spin Textures in Fe/Gd Based Multilayer Thin Films." Microscopy and Microanalysis, Volume 28, Issue S1, 1 August 2022, Pages 2336-2337

The structure of a novel chiral spin texture is determined by tracking its evolution from striped domain walls. Previous work reported the texture as bound pairs of counter-rotating skyrmions, but subsequent publications presented alternative interpretations of the LTEM data. This work confirms the structure as a pair of counter-rotating skyrmions.

Chapter VI. STEM Holographic Imaging of Magnetic Domains in Fe/Gd Multilayer Thin Films

William S. Parker, Andrew Ducharme, Benjamin J. McMorran, Sergio A. Montoya, Eric E. Fullerton, Fehmi S. Yasin, Xiuzhen Yu. "STEM Holographic Imaging of Magnetic Domains in Fe/Gd Multilayer Thin Films." Manuscript in Preparation.

We use transmission electron interferometry to image magnetic domains in a magnetic multilayer thin film. We place a nanofabricated amplitude splitting diffraction in the C2 aperture of a scanning transmission electron microscope, building on techniques developed previously for reliable STEM holography measurements. The resulting experimental setup provides high quality magnetic images, with ample room for improvement, and is minimally intrusive to the microscope.

CHAPTER II

HYBRID SKYRMIONS IN MAGNETIC MULTILAYER THIN FILMS ARE HALF-INTEGER HOPFIONS

This chapter "Hybrid Skyrmions in Magnetic Multilayer Thin Films are Half-Integer Hopfions" is a manuscript in preparation for submission to Physical Review Letters. A preprint is available on arXiv. I developed the theoretical framework constructing hybrid skyrmions from the Hopf fibration. I derived the properties and behavior of this framework. I performed the micromagnetic simulations, with assistance from Jacques Reddinger, and I performed the image processing and data analysis of the results. The concept of a half-integer Hopfion, with magnetic field lines forming knots on a torus, was developed by Benjamin McMorran with past group members. I wrote the manuscript, with editing from Jacques Reddinger and Benjamin McMorran.

2.1 Introduction

Here, we show that the DW twisting in hybrid skyrmions creates additional topological structure, contributing to their exceptional stability. Specifically, hybrid skyrmions can be modeled as half-integer Hopfions - three-dimensional solitons with Hopf index $\pm 1/2$ - and we show how they can be constructed directly from the Hopf fibration underlying integer Hopfions. Partially twisted DWs lead to a fractional Hopf index between 0 and $\pm 1/2$, which provides an important metric for experimental comparison, allowing topological charge to be related solely to surface-sensitive measurements. The hybrid skyrmions' fractional charge is a result of unsatisfied boundary conditions; while integer Hopfions are localized in three dimensions, hybrid skyrmions are localized in only two, with the geometry of the system constraining the third. This non-localization is a general feature of solitons with fractional charge,

for example two-dimensional magnetic vortices (merons) [25], Bloch points [26], and optical vortices [27].

We use MuMax3 to perform micromagnetic simulations representative of the Fe/Gd multilayer thin films that Desautels *et al.* [18] tuned to host skyrmion lattices at room-temperature and remanence, and numerically calculate the Hopf index of the results. Our results show good agreement between theoretical expectations, previous observations of this material, and simulated magnetization, and reveal the underlying topology of the complex structure of a hybrid skyrmion.

2.2 Background

Magnetic skyrmions are two-dimensional topological solitons - stable, particle-like configurations of the vector field of magnetization. Their non-triviality is captured by a 2D topological index, the skyrmion number $N_{sk} = \frac{1}{4\pi}\int \mathbf{m} \cdot [\partial_x \mathbf{m} \times \partial_y \mathbf{m}]\, dxdy$ where $\mathbf{m}$ is the normalized magnetization vector. This index separates two-dimensional vector fields into equivalence classes which cannot be continuously deformed into each other. In this way, the topological charge corresponds to physical stability, forbidding smooth transformations between skyrmion states and uniform magnetization.

The magnetization configuration of a skyrmion can be described as a closed DW loop, separating an out-of-plane magnetic domain from an antiparallel surrounding region. The magnetization rotates smoothly from within the domain to without, creating an in-plane DW between the two. The orientation of the DW magnetization determines its helicity; Néel-type DWs point normal to the DW itself, while Bloch-type DWs point along the DW. In-plane skyrmion analogs, in which the isolated domain and surrounding region lie in-plane, are called bimerons [28] and have different geometric nuances but equivalent topology. In multilayer thin films, skyrmions have

a hybrid texture, with Bloch-type DWs at the center of the film and Néel-type DWs at the top and bottom surfaces.

Hopfions, or Hopf solitons, are a natural way to extend skyrmions into three dimensions. The configuration of a Hopfion is that of a skyrmion tube - a skyrmion extended trivially along its central axis - wrapped into a torus. Their non-trivial topology is captured by the Hopf index, written in real space as $H = -\frac{1}{(8\pi)^2}\int \mathbf{F}\cdot\mathbf{A}d^3\mathbf{r}$ where $\mathbf{F}$ is the emergent magnetic field and $\mathbf{A}$ its vector potential [15]. Integer-valued magnetic Hopfions take the form of a bimeron tube wrapped into a closed loop around the z-axis, such that the magnetization in the core of the torus is parallel to this axis, while the magnetization outside the torus is antiparallel. In this configuration, the core of the torus is an isolated magnetic domain, and the texture as a whole is localized in three dimensions. These have recently been observed in magnetic systems [29], having been studied previously in other contexts, e.g., high energy physics [30] and superconductivity [31].

Here we generalize the Hopfion model by considering a wider class of 2D topological structures (skyrmions) wrapped azimuthally into a torus. For a hybrid skyrmion, the magnetic configuration can be achieved by wrapping a half-integer skyrmion (meron) in this way (as opposed to the integer-valued bimeron that results in an integer-valued Hopfion). This can be seen in the cross-section of its DW, shown in Fig. 3. This has two remarkable effects. First, the resulting texture has a half-integer Hopf index, since the Hopf index is proportional to this cross-sectional texture's skyrmion number. Second, the texture can be created from the Hopf fibration by treating the fibers of the Hopf map as field lines of the magnetization; that is, creating a magnetization which is everywhere tangent to the Hopf fibration. Physically, the

latter point corresponds to bringing flux closure lines inside the material, allowing the magnetization itself to take on some of the skyrmion's dipolar structure.

2.3 Construction of Hybrid Skyrmions from the Hopf Fibration

The Hopf fibration fills all of real space $\mathbb{R}^3$ with linked torus knots on a set of nested tori, via stereographic projection of the fibers of the Hopf map from the 3-sphere. The vector field of a hybrid skyrmion is formed by taking these torus knots to be its field lines; that is, by constructing a vector field which is at every point in space tangent to the Hopf fiber passing through that point. Fig. 4 shows these fibers as well as the tangent vectors at their highest and lowest points, which form the centers of the skyrmion's DWs. Note the distinction from integer Hopfions: for integer Hopfions, the Hopf fibers define curves along which magnetization is constant, while for hybrid skyrmions the Hopf fibers are everywhere tangent to the magnetization. As a result, in hybrid skyrmions the fibers act as magnetic flux lines, and their knotted structure directly implies their resistance to annihilation.

As shown in Appx. A.1, the Hopf fiber passing through a point (x, y, z) can be written as a parametric curve

$$\mathbf{S}(t) = \frac{1}{1 + R^2 + (1 - R^2)\cos t - 2z \sin t} \times \begin{pmatrix} 2x\cos t - 2y \sin t) \\ 2y \cos t + 2x \sin t) \\ 2z \cos t + (1 - R^2)\sin t \end{pmatrix} \tag{2.1}$$

where $R^2 = x^2 + y^2 + z^2$. The hybrid skyrmion magnetization is given by the normalized tangent vectors to this curve

$$\begin{aligned} \mathbf{m}(x, y, z) &= \frac{\partial_t S(t)}{|\partial_t S(t)|}\Big|_{t=0} \\ &= \frac{1}{1 + R^2} \begin{pmatrix} 2(xz - y) \\ 2(yz + x) \\ 1 + z^2 - x^2 - y^2 \end{pmatrix}. \end{aligned} \tag{2.2}$$

1/2-Integer Hopfion
3D Topological Index: ±1/2
Localized in xy

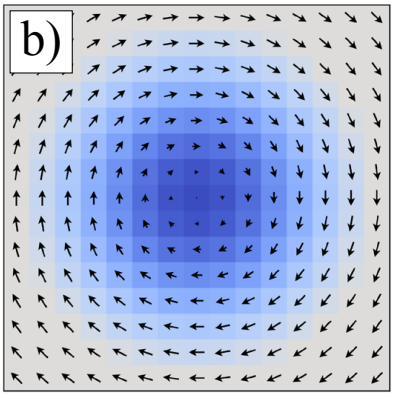

Cross-section texture:
Meron
2D Topological Index: ±1/2
Not localized in 2D

Integer Hopfion
3D Topological Index: ±1
Localized in xyz

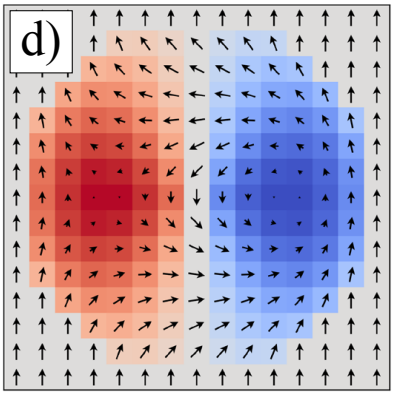

Cross-section texture:
Bi-meron
2D Topological Index: ±1
Localized in 2D

Figure 3. Schematic of a) a hybrid skyrmion, or 1/2-integer Hopfion, and c) an integer Hopfion. The hybrid skyrmion is composed of a b) meron wrapped around the vertical axis, resulting in an isolated magnetic domain along the vertical axis, and is therefore localized only in x and y. The hopfion is composed of a d) bimeron wrapped around the vertical axis, resulting in a ring-shaped isolated magnetic domain, and is therefore localized in x, y, and z. The meron has 1/2-integer skyrmion number, while the bimeron (an in-plane skyrmion analogue) has an integer skyrmion number, which explains the 1/2-integer and integer 3D topological charges of the hybrid skyrmion and the Hopfion, respectively.

Since this vector field is cylindrically symmetric, it is useful to express it in cylindrical coordinates (ρ, ϕ, z)

$$\mathbf{m}(\rho, \phi, z) = \frac{1}{1+\rho^2+z^2} \begin{pmatrix} 2\rho(z\cos\phi - \sin\phi) \\ 2\rho(z\sin\phi + \cos\phi) \\ 1+z^2-\rho^2 \end{pmatrix}. \tag{2.3}$$

Eq. (2.3) is a unit vector field in $\mathbb{R}^3$ which at every point is tangent to the Hopf fiber passing through it. A similar structure has been found as a solution to a certain class of equations in magnetohydrodynamics [32], but in that case the tangent was taken prior to stereographic projection, yielding a vector field whose magnitude falls to zero far from the origin and is therefore truly localized.

2.3.1 Properties and Behavior. At $z = 0$, Eq. (2.2) has the form of a Bloch-type skyrmion in the xy-plane. The magnetization rotates from $\mathbf{m} = +\hat{\mathbf{z}}$ at the origin to $\mathbf{m} = -\hat{\mathbf{z}}$ far from the origin, rotating around $\hat{\rho}$ such that all in-plane components are azimuthal. In this plane, the maximum in-plane magnetization is found at $\rho = 1$.

$$\mathbf{m}(x, y, 0) = \frac{1}{1+x^2+y^2} \begin{pmatrix} -2y \\ 2x \\ 1-x^2-y^2 \end{pmatrix}. \tag{2.4}$$

Away from $z = 0$, the polarization of the skyrmion - that is, the limits as $\rho \to 0, \infty$ - remains the same but the in-plane components rotate, becoming more radial farther from $z = 0$. As z increases, the in-plane components twist radially outward, creating a Néel-type skyrmion, while as z decreases, they twist radially inward, creating a Néel-type skyrmion of the opposite helicity. These helicities match the flux closure curves created by the dipole field of the skyrmion's core and surrounding region and are known as Néel caps.

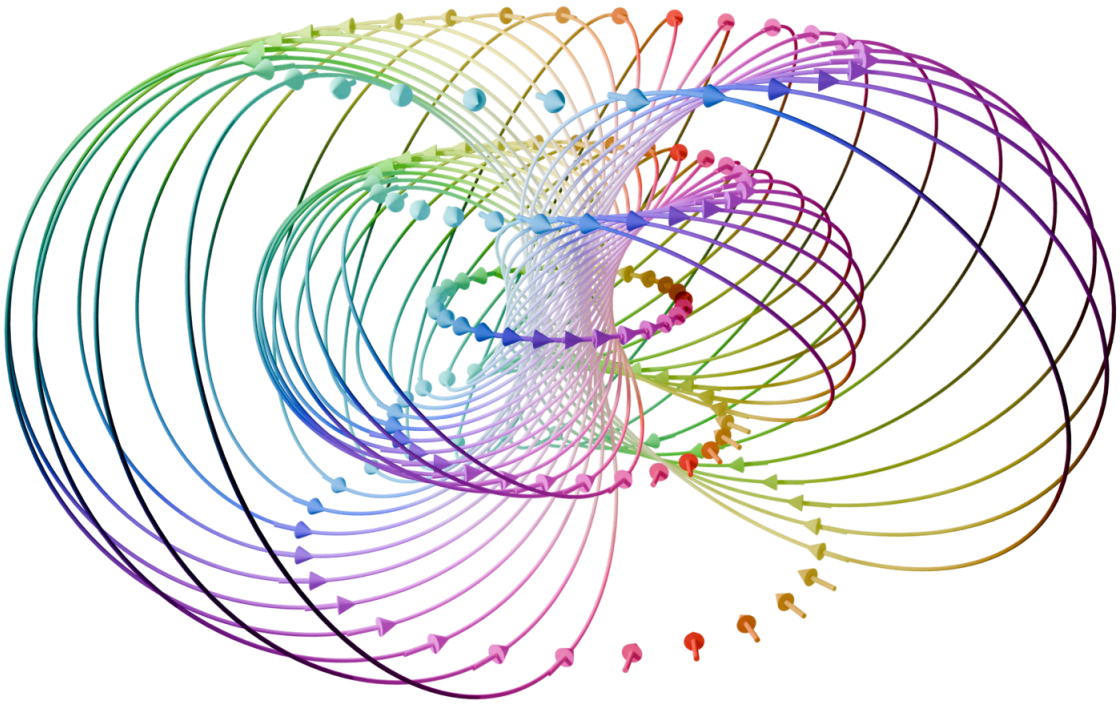

Figure 4. The Hopf fibration in real space. Tangent vectors are plotted at the highest and lowest points of the fibers, where they lie in-plane. These points correspond to the DW center at a given z.

The helicity of the skyrmion can be expressed exactly as a function of z. To do so, we define helicity α as the angle between the in-plane component of magnetization $\mathbf{m}_\perp = m_x\hat{\mathbf{x}} + m_y\hat{\mathbf{y}}$ and the in-plane gradient of m_z, $\nabla_\perp m_z = \partial_x m_z\hat{\mathbf{x}} + \partial_y m_z\hat{\mathbf{y}}$ [33]. With this definition, pure Néel-type skyrmions have helicity either 0 or π, while pure Bloch-type skyrmions have helicity $\pi/2$ or $3\pi/2$. Calculated explicitly from Eq. (2.2), α has the form

$$\alpha(z) = \cos^{-1}\left(\frac{-z}{\sqrt{1+z^2}}\right). \tag{2.5}$$

which varies from 0 to π as z varies from $-\infty$ to ∞.

In contrast to simulated and experimentally observed hybrid skyrmions, the radius of the Hopf-derived hybrid skyrmion ρ_{DW} - the radius at which the in-plane component is maximized - expands as $|z|$ increases, varying as

$$\rho_{DW} = \sqrt{1+z^2}. \tag{2.6}$$

Micromagnetic simulations show that hybrid skyrmions' DWs are typically barrel-shaped [22]. As this qualitative difference can be rectified by a smooth coordinate rescaling, it has no impact on the topology of the structure, which is instead determined by the DW helicity.

Lastly, we can calculate the curves along which $\mathbf{m}$ is constant - that is, the fibers of the hybrid skyrmion. These are given implicitly by

$$\begin{aligned} x &= x_0 - y_0 z \\ y &= y_0 + x_0 z. \end{aligned} \tag{2.7}$$

For any fixed $\rho_0 = \sqrt{x_0^2 + y_0^2}$, these lines, as shown in Fig. 8, are the generators of the hyperboloid $\rho = \rho_0\sqrt{1+z^2}$; for example, the hyperboloid given by the skyrmion radius in Eq. (2.6) when $\rho_0 = 1$. Fig. 8(a) shows these curves for the DWs ($\rho_0 =$

1), while Fig. 8(b) shows the same, calculated numerically, for a simulated hybrid skyrmion.

This last result sheds some light on the hybrid skyrmion's non-integer Hopf index. For integer Hopfions, the fibers form closed loops, with a linking number equal to the Hopf index; however, the fibers of Eq. (2.7) extend to infinity, never closing on each other. Since stereographic projection maps all infinities in $\mathbb{R}^3$ to a single point in $\mathbb{S}^3$, and the Hopf-derived hybrid skyrmion is not homogeneous at infinity, the hybrid skyrmion is not only many-to-one, but also one-to-many. In fact, the pole of $\mathbb{S}^3$ corresponding to infinity in $\mathbb{R}^3$ itself covers all of $\mathbb{S}^2$. In other words, a hybrid skyrmion's magnetization approaches a different value far from the origin depending on which direction away from the origin you travel; this incongruity expresses the non-localization of a hybrid skyrmion in 3D. In reality, the hybrid skyrmion is localized in z by the finite thickness of the host system.

2.3.2 Hopf Index. The Hopf index of a vector field $\mathbf{m}(x, y, z)$ can be calculated explicitly using its real-space expression [15]

$$H = -\frac{1}{(8\pi)^2} \int \mathbf{F} \cdot \mathbf{A} d^3\mathbf{r} \tag{2.8}$$

where $F_i = \epsilon_{ijk}\mathbf{m} \cdot (\partial_j \mathbf{m} \times \partial_k \mathbf{m})$ and $\nabla \times \mathbf{A} = \mathbf{F}$ are additionally defined based on $\mathbf{m}$. $\mathbf{F}$ can be seen as the emergent magnetic field, and $\mathbf{A}$ its vector potential [29].

We can parameterize the magnetization in a natural way by azimuthal and polar angles Φ and Θ, respectively: $\mathbf{m} = (\sin\Theta\cos\Phi, \sin\Theta\sin\Phi, \cos\Theta)$. When Θ is independent of ϕ and Φ has the form $\Phi = Q\phi + h(\rho, z)$ (for some integer Q and some function $h(\rho, z)$ which is independent of ϕ), the Hopf index can be expressed in

the form [34]

$$\begin{aligned} H &= \frac{Q}{4\pi}\int_{-\infty}^{\infty} dz \int_{0}^{\infty} dr \sin\Theta \left(\frac{\partial\Theta}{\partial\rho}\frac{\partial h}{\partial z} - \frac{\partial\Theta}{\partial z}\frac{\partial h}{\partial\rho} \right) \\ &= Q \times N_{\rho z} \end{aligned} \tag{2.9}$$

where $N_{\rho z}$ is the skyrmion number of the toroidally wrapped texture, and Q is the winding number around the z axis. Here, the Hopf index takes the explicit form of the product of these two quantities. As noted above, for hybrid skyrmions the toroidally wrapped texture is a meron, with half-integer charge, while for integer Hopfions the toroidally wrapped texture is a bimeron, with integer charge. Θ and Φ can be calculated directly from our Hopf-derived model of the hybrid skyrmion, Eq. (2.3), and $Q = \partial_\phi \Phi = 1$, giving an analytical solution for H:

$$\begin{aligned} H &= \frac{1}{4\pi}\int_{-\infty}^{\infty} dz \int_{0}^{\infty} dr \left(-\frac{4\rho}{(1+z^2+\rho^2)^2} \right) \\ &= -\frac{1}{2} \end{aligned} \tag{2.10}$$

Note that in the construction of $\mathbf{m}$, Eq. (2.2), we had a choice of two directions for the Hopf fibers' tangent vectors; making the opposite choice results in $H = +1/2$. Like the skyrmion index, the sign of the Hopf index depends on the polarity of the spin texture.

2.3.3 Hopf index of partially twisted skyrmions. In real systems, the Néel caps arise from a layer dependent interaction competing with naturally Bloch-type domain walls. As a result, the surfaces of the material are not necessarily completely Néel-type, but instead retain some azimuthal component. In addition, when the system contains inherent DMI, the Bloch core may be displaced above or below the center of the film [22]. Here, we consider the Hopf index of such a partially twisted, possibly asymmetric, hybrid skyrmion by recalculating the Hopf index with restricted limits of integration.

If we restrict the integration w.r.t. z in Eq. (2.10) to a lower limit z_l and an upper limit z_u, we find that

$$H = \frac{\tan^{-1}(z_l) - \tan^{-1}(z_u)}{2\pi}. \tag{2.11}$$

We can rewrite this in terms of the helicity at the surfaces by solving for z in Eq. (2.5), and substituting the result into Eq. (2.11), giving

$$H = \frac{\tan^{-1}(\cot(\alpha_u)) - \tan^{-1}(\cot(\alpha_l))}{2\pi}, \tag{2.12}$$

where α_l, α_u are the helicities at z_l, z_u, respectively. In the symmetric case $z_l = -z_u$, the Hopf index is given in terms of helicity by

$$H = \frac{\tan^{-1}(\cot(\alpha_u))}{\pi} \tag{2.13}$$

This means the Hopf index varies continuously from 0 when the skyrmion is uniform throughout the thickness, to $\pm 1/2$ when the skyrmion twists to fully Néel-type at the surfaces. For a texture where the Bloch walls twist only partially toward Néel-type at the surface, the Hopf index is between 0 and $\pm 1/2$. Furthermore, in this case, the Hopf index depends solely on the helicity at the surface. This is an important result for the experimental characterization of hybrid skyrmions, as it means the 3D topological charge can be understood using only surface-sensitive magnetic imaging - provided the texture is known to have this hybrid structure - without the need to quantitatively measure the full 3D magnetization.

2.4 Micromagnetic Simulations

To assess the validity of these results in the context of a well-studied system, we numerically solved the Landau-Lifshitz-Gilbert (LLG) equation using MuMax3 [14]. The material parameters were chosen to match those obtained experimentally by Montoya et. al in [21], which are representative of an Fe/Gd multilayer thin film, and temperature was set to 300 K. A 1.28 µm $\times$1.28 µm $\times$80 nm slab was initialized with

random magnetization. A saturating perpendicular field of -330 mT was initialized, then decreased in increments of 5 mT, with the LLG equation evolved for 15 ns at each field step. This procedure generates a stable mixture of worm domains and skyrmions at remanence.

Next, we simulated a field sweep from remanence back to negative saturation, allowing us to predict the behavior of the Néel caps and associated evolution of the Hopf index of a hybrid skyrmion as they varied with applied field. The applied field was decreased in steps of 5 mT from remanence, and the LLG equation evolved for 15 ns at each field step, until all magnetic domains were annihilated at -325 mT.

Additionally, the magnetization after the -250 mT field step was used as a seed for a high-resolution simulation using the `relax()` function of MuMax3, which disables precession in the LLG equation to instead attempt to find the energetic minimum [14]. This method produces a less noisy result, while preserving the structure. At -250 mT, all domains have shrunken to isolated skyrmions, so this additional simulation allows for a closer examination of the structure of an individual hybrid skyrmion.

2.5 Results

Fig. 5 shows the surface magnetization of the simulation result at remanence. As expected, the DWs are nearly Néel-type, but not fully, competing energetically with the azimuthal component at the center of the film. At remanence, we see primarily worm domains, with three skyrmions - two left-handed and one right-handed. To quantify the twist of each skyrmion, the surface helicity was averaged for a circular region encompassing the skyrmion, weighted by the magnitude of the in-plane component of magnetization. Eq. (2.13) was then used to predict the Hopf index we should expect based on the surface helicity. The Hopf index was

	A	B	C
Avg. Surface Helicity	0.8804π	0.8843π	-0.8757π
Helicity-based HI (Eq. (2.13))	-0.3804	-0.3843	0.3757
Numerically-calculated HI	-0.3909	-0.3831	0.3495

Table 1. The average surface helicity, surface-helicity based Hopf index (calculated using Eq. (2.13)), and numerically calculated Hopf index of the simulated skyrmions shown in Fig. 5.

also calculated numerically from the full vector magnetization using the procedure described in Appx. A.2, and shows a good match to the value predicted by Eq. (2.13). Table 1 summarizes these results.

Next, a field sweep from remanence to saturation was simulated, using the magnetization shown in Fig. 5(d) as a seed. The field was decreased in steps of 5 mT, and the LLG equation evolved for 15 ns at each step, until all domains were annihilated at a field value of -325 mT. At each step, the skyrmion's surface helicities and numerical Hopf index were calculated, with its center tracked by the weighted average of its core magnetization. Fig. 6(a) shows the calculated average surface helicities at the upper and lower surfaces of the film, and Fig. 6(b) shows the Hopf index expected from these surface helicities, along with the explicitly calculated Hopf index. Fig. 6(c) shows the z-dependent average helicity for three different field values: remanence, the value at which surface helicity was closest to Néel-type, and the last field step before annihilation.

Notably, the Néel caps are most Néel-type at around -220 mT, rather than near remanence or saturation. At remanence, the DWs of neighboring magnetic domains are pressed together (Fig. 7(a)), and their Néel caps antiparallel, making it energetically unfavorable for the DWs to twist fully Néel-type. As the magnitude of applied field is increased, skyrmions become more isolated (Fig. 7(b)), allowing their Néel caps to twist more fully. However, the skyrmions also shrink with applied field,

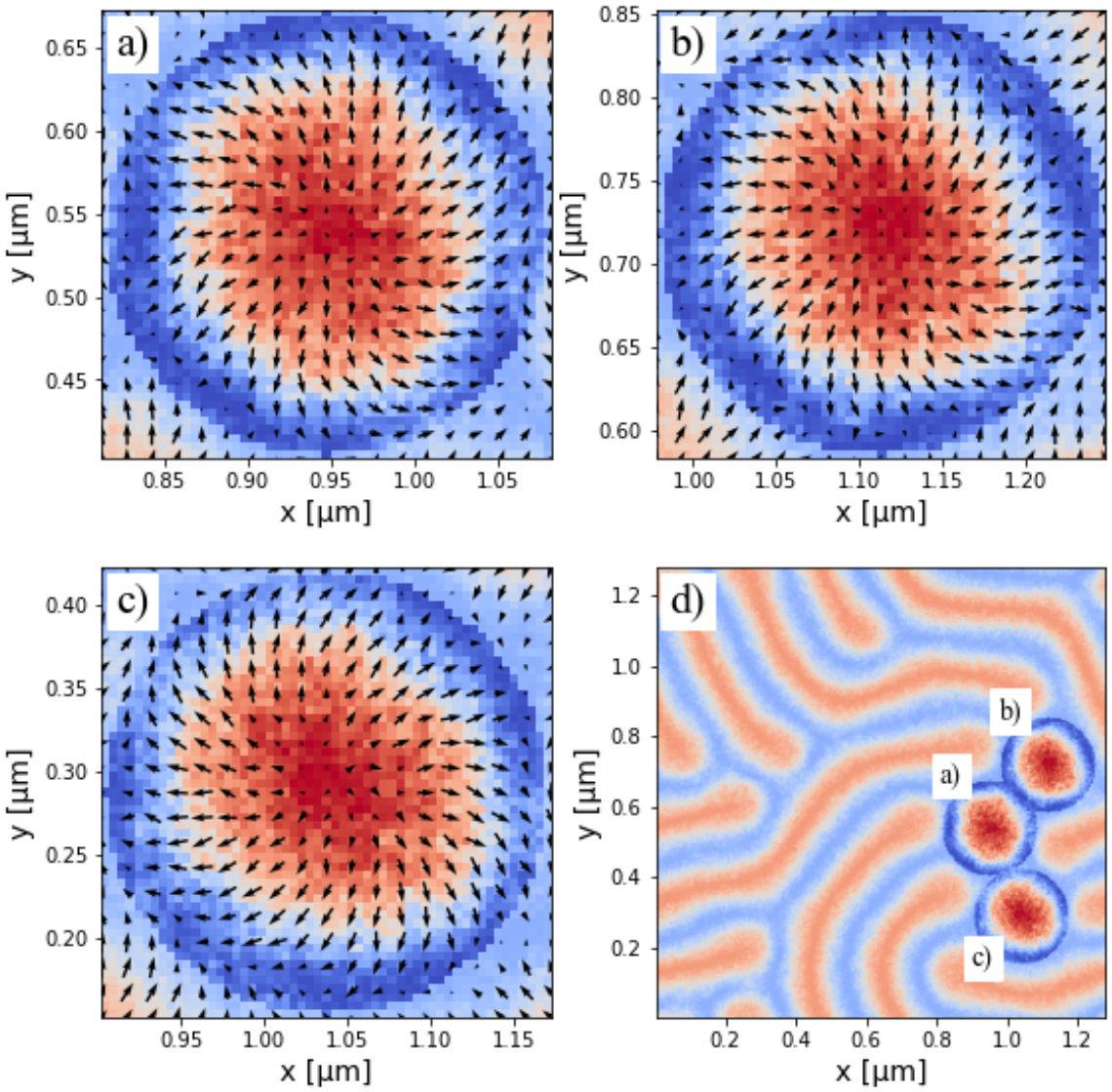

Figure 5. Simulated surface magnetization of three hybrid skyrmions stabilized at remanence. This surface helicity represents the Néel cap, which retains some of the azimuthal component at the center of the film, which is left-handed in a) and b), and right-handed in c).

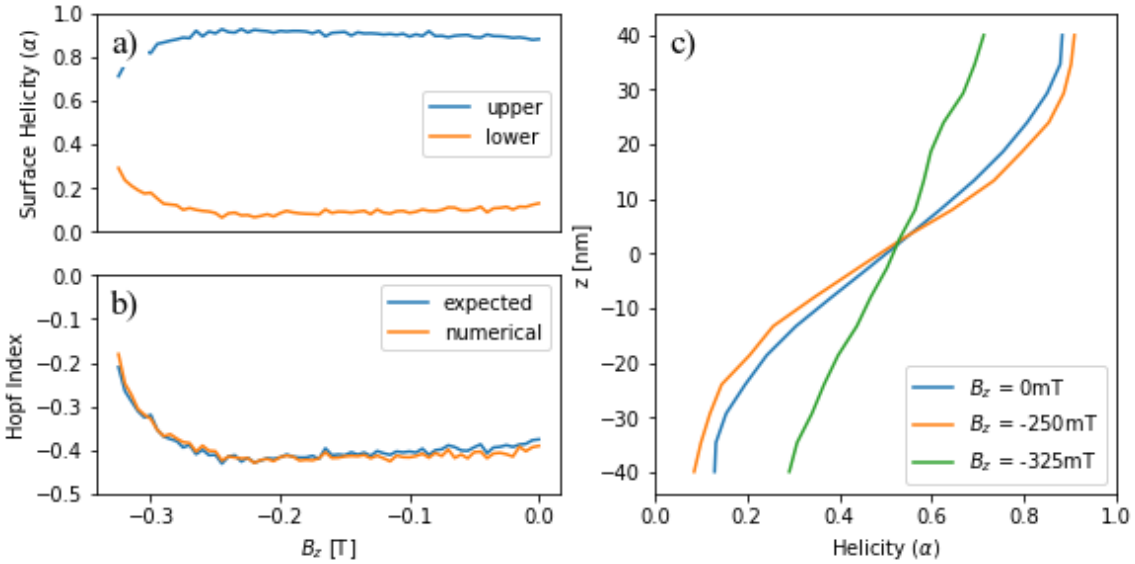

Figure 6. Evolution of (a) surface helicity and (b) Hopf index of the simulated skyrmion as B_z is decreased from remanence to -325 mT. (c) shows the average helicity through the thickness of the skyrmion for three applied field values.

until the DWs on opposite sides of an individual skyrmion begin to interact (Fig. 7(c)), again creating a preference against fully twisted Néel caps.

Finally, the -250 mT magnetization, after relaxation to a minimum energy state, was used to numerically calculate the curves of constant magnetization for a hybrid skyrmion. Fig. 8(a) shows these curves for the half-integer Hopfion constructed from the Hopf fibration, Eq. (2.2), and Fig. 8(b) shows the numerically calculated results for a simulated hybrid skyrmion. The simulated hybrid skyrmion's DWs are barrel-shaped rather than hyperboloid, but can be created from the former's via a smooth rescaling of radial coordinates. This barrel shape is also predicted by [22]. The salient feature is the nearly 180^{o} rotation from top to bottom, which corresponds to the varying helicity.

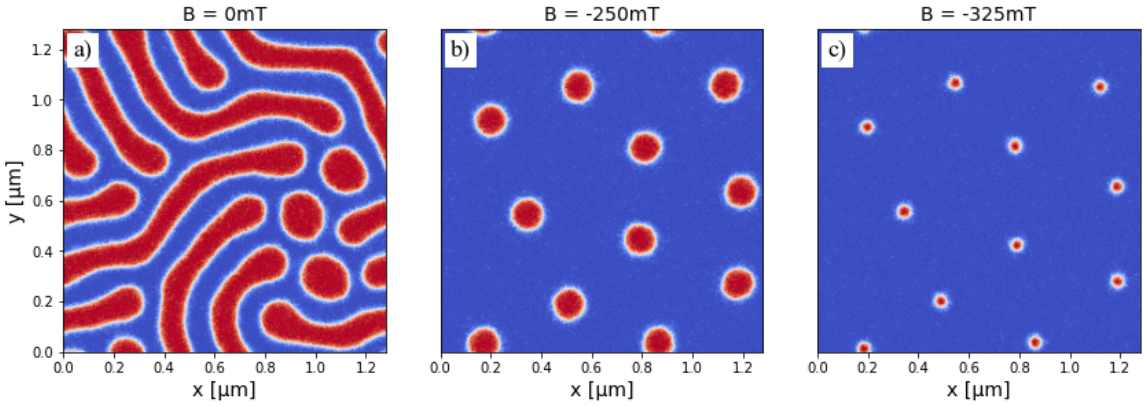

Figure 7. Z-component of magnetization at the center of the film at a) remanence, b) -250 mT, and c) -325 mT.

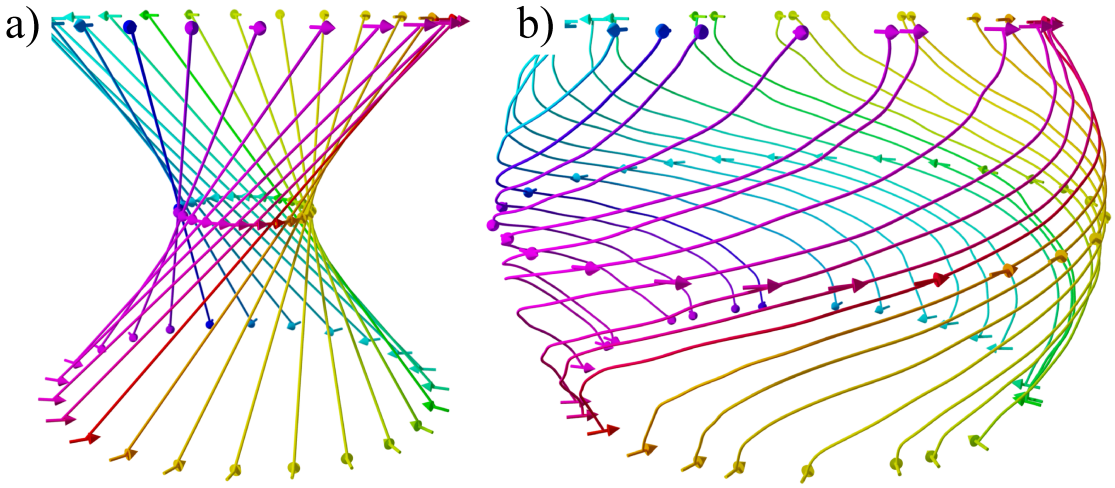

Figure 8. Curves of constant magnetization for (a) the skyrmion constructed from the Hopf fibration, Eq. (2.2), and (b) the simulated isolated hybrid skyrmion, starting from points at the center of the DW. Note how the curves wrap almost but not quite 180^{o} around the z-axis; this is equivalent to the nearly 180^{o} twist in helicity from top to bottom. The z-dependence of this wrapping matches the z-dependence of its helicity (Fig. 6(c), B_z=-0.250 T), varying fastest at the center and slowing near the surfaces.

2.6 Chapter Conclusion

In this chapter, we showed that the additional twisting of hybrid skyrmions creates a knotted topological structure. In particular, hybrid skyrmions have a half-integer Hopf index, adding another non-trivial topology to the plethora of topological spin textures observed in magnetic systems. We also showed that the structure of a hybrid skyrmion can be constructed directly by creating a vector field tangent to the fibers of the Hopf fibration. This has the physical interpretation of tying magnetic field lines into linked torus knots, creating a barrier against the annihilation of the structures. We used micromagnetic simulations to tie these results to a well known and highly promising system, Fe/Gd multilayers, in order to understand the underlying topology first at remanence as well as in the presence of an external field. A relation to surface helicity was derived, providing a way to connect topology to real-world experiments. The next chapter expands on this, using a surface-sensitive technique to quantify surface helicity in Fe/Gd multilayers, and combining it with projective techniques to fully characterize hybrid skyrmions' 3D structure.

CHAPTER III

REAL SPACE IMAGING OF HYBRID SKYRMION TEXTURES IN MAGNETIC MULTILAYER THIN FILMS

This chapter "Real Space Imaging of Hybrid Skyrmion Textures in Magnetic Multilayer Thin Films" is a manuscript in preparation for submission to Physical Review B. Benjamin McMorran conceived of the imaging combination and oversaw the data collected by SEMPA. Sergio Montoya and Eric Fullerton developed and studied these materials in detail. Sergio Montoya fabricated all the samples used. I analyzed the SEMPA data for helicity measurements. I collected and analyzed the LTEM data, and developed a ridge-detection workflow to allow for helicity measurements of LTEM data. I performed the micromagnetic simulations and analyzed the results. The SEMPA data was collected before my time in the group, and multiple past group members have contributed to our ability to use and analyze it. I wrote the manuscript.

3.1 Introduction

Studies of magnetic multilayer thin films rely generally on either X-ray [20, 29, 35], neutron [11, 23, 36], or electron microscopy techniques [12, 21, 37]. X-ray techniques access the out-of-plane magnetization and have been instrumental in the development of room-temperature skyrmion lattices, but they are projective and lack the resolution to observe many chiral spin textures, typically relying on reciprocal space measurements to understand magnetic phases across large regions. Neutron techniques were the first to provide an observation of skyrmions, in B20-structured MnSi single crystals [11]. More recently they have been used in conjunction with micromagnetic modeling to provide an understanding of the 3D hybrid skyrmion structure, and these provide a depth-dependent profile of helicity. However, they

depend on the interpretation of scattering data, and provide no xy-dependent information of the magnetic structure. LTEM provides real-space measurements, at the resolutions required to image most skyrmion systems, but it only accesses the in-plane magnetic induction - and worse, is then only sensitive to the Bloch component of DWs.

In this paper, we combine LTEM with the relatively unique technique called scanning electron microscopy with polarization analysis (SEMPA) [38] to understand the real-space structure of skyrmions in Fe/Gd magnetic multilayer thin films. LTEM measures the Aharonov-Bohm phase acquired by fast, plane-wave electrons passing through a sample; or equivalently, their spatially dependent deflection due to the Lorentz force. It is thus sensitive to the in-plane magnetic field, integrated through the sample, but contrast is formed only by the Bloch component of domain walls. SEMPA analyzes the spin polarization of secondary electrons emitted by the sample under illumination by a focused SEM probe to image all three components of surface magnetization (1 nm probe depth), allowing us to verify the existence of Néel caps. By combining the two, we experimentally determine the real-space 3D structure of the hybrid skyrmion. We perform micromagnetic simulations for a better understanding of the full structure and use these micromagnetic results for quantitative comparison against our experimental findings. Combined, the two provide a complete picture of the hybrid skyrmion's structure.

3.2 Experimental Procedure

The Fe/Gd multilayers were fabricated following the process described in [21]. Alternating layers of Fe and Gd were sputter deposited in an ultrahigh vacuum (UHV) environment at room temperature. 5 nm of Ta or Pt was used as both a seed and capping layer to prevent sample oxidation. For SEMPA imaging, the films were

deposited on a Si substrate; for LTEM, they were deposited on a SiN membrane layered across a square window on a Si TEM grid. Once inserted into the SEMPA, the instrument's focused ion beam was used to remove the top capping layer of Ta. Since SEMPA is a UHV instrument, oxidation after removal of the capping layer is not a concern.

To achieve a remanence magnetic state with a high density of skyrmions, a variety of applied field sequences can be used. Previous works have reportedly generated a skyrmion lattice by first applying a saturating field 45° from out-of-plane, then returning to remanence to create ordered chiral stripes, then increasing the field directly out-of-plane until the stripes break up into skyrmions - in that case, 190 mT - before finally returning to remanence [18]. However, other field sequences can achieve a similar effect; for example, applying a 190 mT field out-of-plane, then tilting the sample within this field up to 40°, and then back to -5°, then removing the field while at -5°, before finally decreasing tilt to 0° (i.e., for imaging in LTEM). This can also yield a hexagonal skyrmion lattice at remanence, although true long-range order is difficult to achieve by either sequence. The LTEM samples present an additional complication because the SiN membranes on which the thin film is deposited must span a vacuum region for transmission imaging. In these vacuum regions, the membrane may be stretched and deformed, and as a result, different regions of the sample respond very differently to a given field sequence - yielding skyrmions, chiral stripes, worm domains, or achiral stripes simultaneously.

Magnetic induction images were acquired using the FEI Titan 80-300 keV field emission microscope at University of Oregon's CAMCOR facility, operating at 300 keV. In Lorentz mode, the objective lens - which typically subjects the sample to a magnetic field - is deactivated and replaced by the Lorentz lens above it. The

objective lens can then be used to controllably apply a magnetic field; to change the direction from out-of-plane, the sample is tilted within the microscope. This setup allows for live imaging while a field sequence is applied. Defocused images were taken at remanence, and the magnetic induction was reconstructed using the single-image transport of intensity equation (SITIE) described in [39].

Surface magnetization images were acquired using the SEMPA instrument located at NIST Gaithersburg, which has since been relocated to University of Oregon's CAMCOR facility. The instrument consists of a commercial UHV SEM with a custom electron polarization analysis detector, as well as a focused ion beam (FIB), used to remove any anti-oxidation capping layer prior to imaging the surface. To measure magnetization, the focused electron beam is rastered across the sample, as in normal SEM imaging, and the secondary electrons emitted from the sample are pulled into a Mott-scattering-based spin-polarization detector. The spin of the emitted secondary electrons can then be directly related to the magnetization at the source of their emission. Two passes are made: the first measuring m_x vs. m_z, and the second m_x vs. m_y. The redundant measurements of m_x are then used to align all three components. All measurements were conducted at room-temperature and with no applied field.

Micromagnetic simulations were performed using MuMax3 to numerically solve the Landau-Lifshitz-Gilbert (LLG) equation [14]. This GPU-accelerated program was run on an Nvidia Ampere A100 GPU in University of Oregon's high-performance compute (HPC) cluster, Talapas. A $1.28 \times 1.28 \times 0.08$ µm slab with $5 \times 5 \times 5$ nm voxels was initialized with a random magnetization, and a -330 mT out-of-plane magnetic field applied. The field was increased to remanence in 5 mT increments, evolving the LLG equation for 15 ns at each step, using magnetic parameters $M_s = 4 \times 10^5$ A/m,

$K_U = 4 \times 10^4$ J/m^3, and $A = 5 \times 10^{-12}$ J/m, which were obtained experimentally in [21]. After the final 15 ns relaxation at remanence, the magnetization was stretched onto a new mesh with $5 \times 5 \times 1$ nm voxel size, to match the 1 nm probe depth of SEMPA to the top layer of magnetization and relaxed for another 15 ns.

3.3 Results

Fig. 9 shows a representative skyrmion from the SEMPA data, the LTEM data, and micromagnetic simulations. The skyrmions found in SEMPA, Fig. 9(a), show mostly Néel-type DWs, while the skyrmions found in LTEM, Fig. 9(b), show a strong Bloch-type DW component. The Néel caps are not fully radially outward, instead retaining some Bloch component. This is expected, as Néel caps compete energetically with the naturally Bloch-type DWs.

To compare simulation to SEMPA data, we look at the top 1 nm layer of simulated magnetization (Fig. 9(c)); the probing depth of the actual SEMPA instrument is roughly 1 nm [40]. To compare simulation to LTEM data, we calculated the Aharonov-Bohm phase imparted on a plane incident electron wave by the full magnetization, following the computations of Mansuripur [41], and used this phase to simulate a defocused (aka, Lorentz) TEM image of the sample. We then applied SITIE to this defocused image to reconstruct the magnetic induction (Fig. 9(d)).

The characterizing feature of hybrid skyrmions is their DW helicity, which is expected to vary from mostly radially inward Néel-type at the bottom surface, to Bloch-type in the core, to mostly radially outward Néel-type at the top surface (assuming a skyrmion with positive m_z core). Quantitatively, helicity is the angle between the in-plane magnetization $m_\perp = m_x\hat{x} + m_y\hat{y}$ and the normal to the DW (by convention pointing from negative m_z to positive m_z), shown in Fig. 10(p). With this convention, Néel-type DWs have a helicity of 0 or π (normal to the DW), while

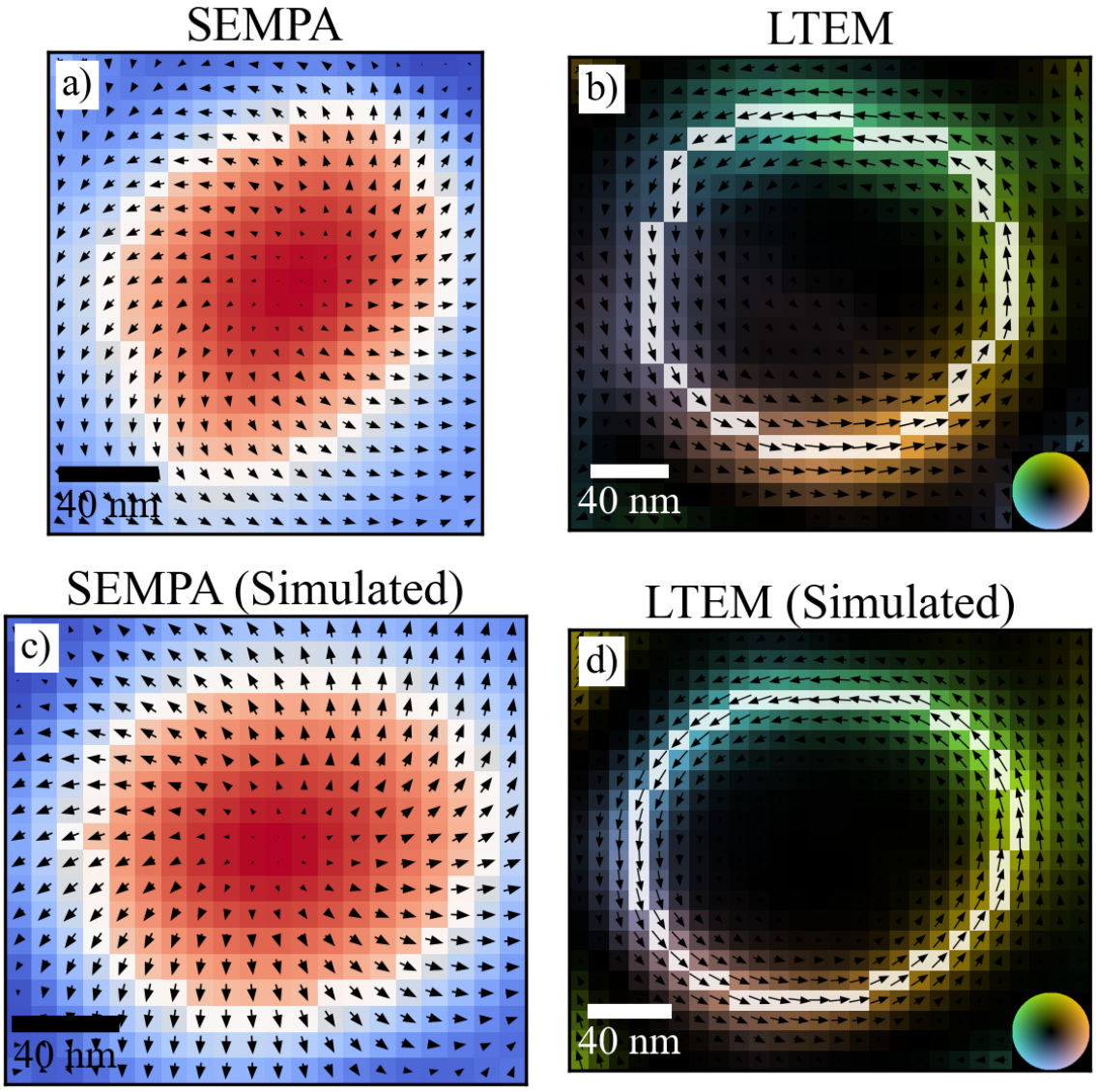

Figure 9. A representative skyrmion from (a) SEMPA, (b) LTEM, and (c), (d) simulation. (a) shows the magnetization directly measured by SEMPA, with m_z in color, and m_x, m_y in arrows. (b) shows the magnetic induction (in-plane magnetic field, integrated through z) measured by LTEM. (c) shows the top, 1 nm layer of simulated magnetization, and (d) shows the simulated magnetic induction from (c) (using all layers of the simulated magnetization, not only the top). In (b) and (d), color represents the direction of in-plane induction, and brightness represents its magnitude.

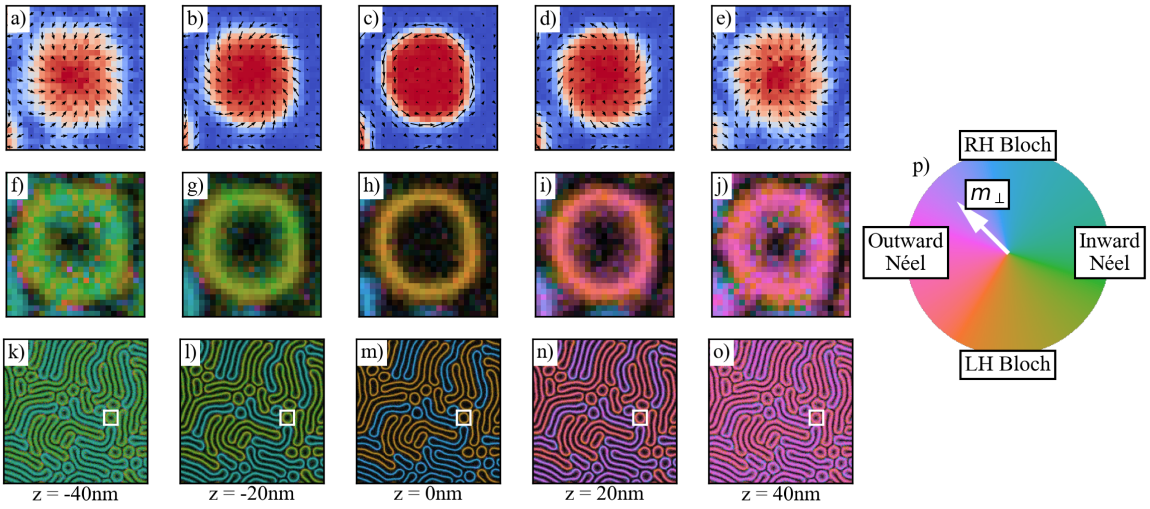

Figure 10. Layer dependence of the simulated magnetization. (a-e) show the magnetization of one skyrmion from the bottom to the top layer. (f-j) show the helicity of the skyrmion, and (k-o) show the helicity of the full region, with the inscribed square showing the location of (a-j). (p) shows how helicity is calculated. The angle between DW magnetization $m_\perp$ and the DW normal is the helicity. In (f-o), brightness represents the magnitude of $m_\perp$. Note that if the polarity of the skyrmion switched (that is, the core pointed down instead up of), then RH/LH Bloch would be switched, and Inward/Outward Néel would be switched.

Bloch-type DWs have a helicity of $\pm\pi/2$ (tangent to the DW). Fig. 10(a-o) shows the variation in helicity from the bottom surface to the top surface, for the simulated magnetization.

Fig. 11 shows how the simulated magnetization's helicity varies from bottom to top, for each of the skyrmions found. For SEMPA data, OpenCV was used to trace contours on $m_z = 0$ to find the DW pixels and DW normals. In LTEM, we measure the magnetic induction $B_\perp$ rather than the magnetization. However, since LTEM lacks B_z information, we used a ridge detection algorithm [42, 43] on $|B_\perp|$ to trace the skyrmion DWs and find their normals. The sign of B_z was determined based on field history.

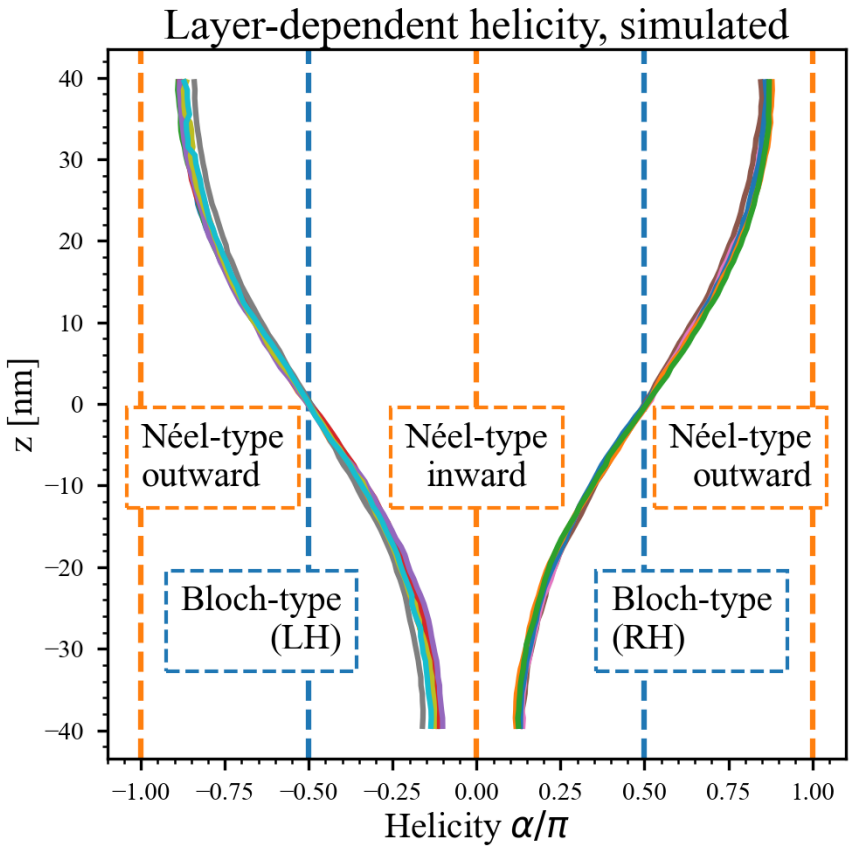

Figure 11. Layer-dependent helicity of the simulated magnetization. At each layer, for each skyrmion, m_z was used to find the DW contour. Helicity was averaged along the contour, giving the average helicity for that skyrmion, for that layer. For each skyrmion, the helicity varies smoothly from nearly Néel-type, radially inward, at the bottom of the film, to nearly Néel-type, radially outward, at the top, passing through perfectly Bloch-type at the center.

Fig. 12 shows the results of the helicity calculations. DW contours are overlayed on SEMPA and LTEM data, and simulated SEMPA and LTEM data, in the left and middle columns. The distribution of helicity is calculated first by each skyrmion's average helicity, and second using all DW pixel points. For each, we see a bimodal distribution, split between left- and right-handed skyrmions, which is possible in these materials due to the lack of symmetry-breaking mechanisms such as DMI. As expected, the SEMPA data shows mostly Néel-type DWs, pointing from positive m_z to negative m_z, with average helicities centered around -0.83π and 0.80π for LH and RH skyrmions, respectively. LTEM is sensitive only to the Bloch component of DWs, so it naturally shows purely Bloch-type skyrmions, with average helicities centered around $\pm 0.50\pi$. Simulation matches these results, with Néel-type cap helicities centered around $\pm 0.87\pi$ and simulated LTEM helicities likewise around $\pm 0.50\pi$.

Based on [22], we also expect hybrid skyrmions to have hourglass shaped DWs (wide at the surface and narrow at the core), and barrel shaped cores (smaller at the surface and larger at the core). For DW width, quantitative comparison between SEMPA and LTEM is not meaningful, as SEMPA measures magnetization while LTEM measures magnetic field. However, we see in simulation that the DWs are narrower in the core and wider at the surface (Fig. 10(a-e)), and we see in experiment that LTEM measures relatively narrow DW magnetic fields relative to the DWs found in SEMPA.

For skyrmion core width, however, quantitative comparison is possible since this depends solely on the center of the DW, which we can identify in both SEMPA and LTEM measurements. To quantify core width, an ellipse was fitted to each skyrmion, for both SEMPA and LTEM measurements, and the major and minor axes are shown in Fig. 13. Both experimental and simulated data shows the expected barrel shape,

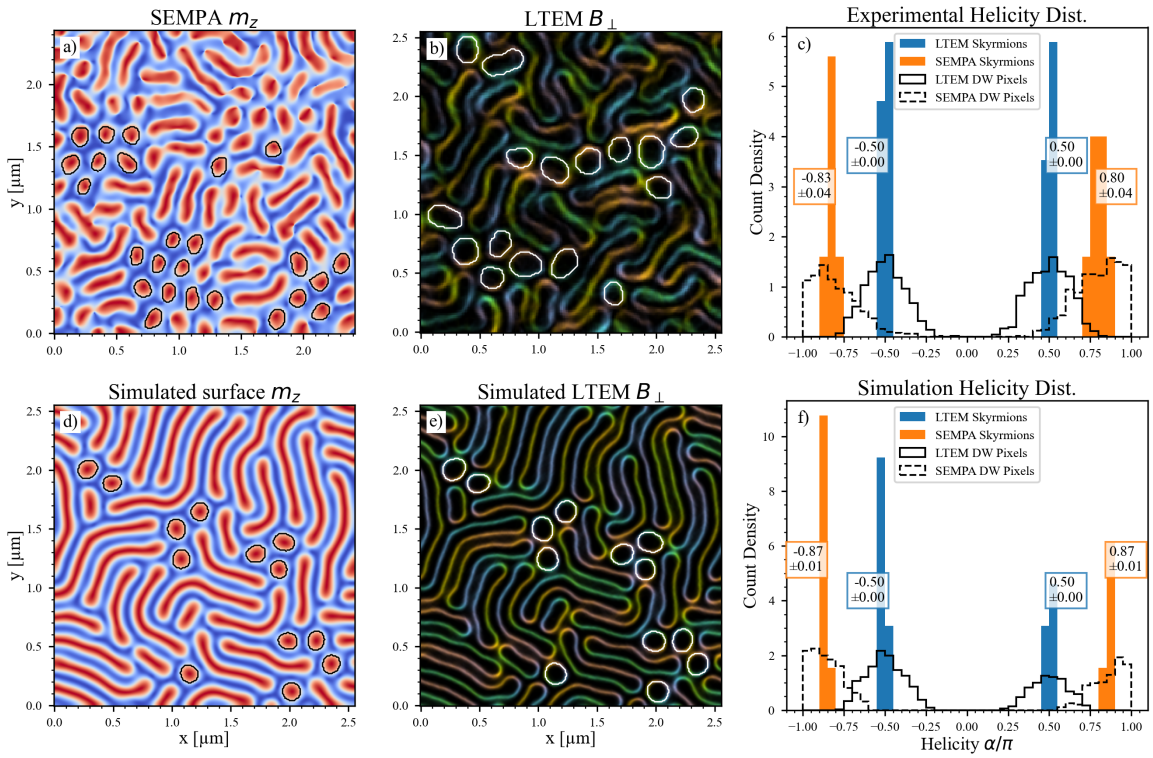

Figure 12. Helicity distribution of skyrmions from SEMPA, LTEM, and simulation. The left column shows skyrmion DWs in (a) the SEMPA data and (d) the top (1 nm) layer of simulated magnetization. Middle column shows skyrmion DWs in (b) the LTEM data and (e) the simulated LTEM data. Right column shows the helicity distributions for (c) experimental and (f) simulated skyrmions. The solid blue and orange histograms show the distribution averaged per skyrmion, and the full distribution of all DW pixel helicities is overlayed in solid and dashed lines for LTEM and SEMPA, respectively.

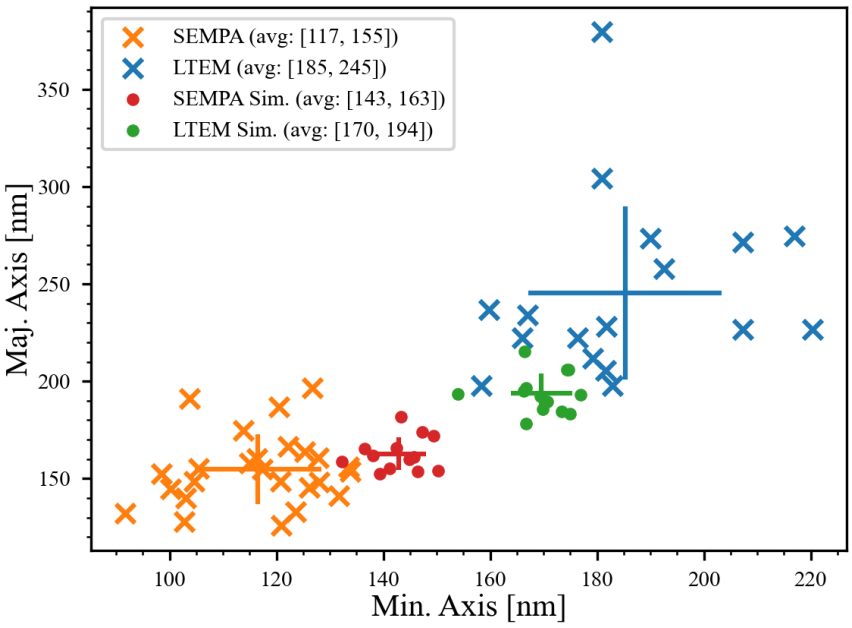

Figure 13. Distribution of skyrmion size by minor and major axes of fitted ellipses. As expected, the surface-sensitive SEMPA measurements detect smaller skyrmions, while the projective LTEM measurements detect larger skyrmions, indicating a barrel-shaped skyrmion. This is more pronounced in the experimental data than in micromagnetic simulations, which could be due to a number of factors, such as the free-standing SiN substrate used in LTEM samples, or heating due to ion milling in SEMPA, or differences in the exact field sequence applied.

with skyrmions found in LTEM wider than those found in SEMPA. The trend is exaggerated in experimental data, which could be due to a number of factors, such as the free-standing SiN substrate used in LTEM samples, heating due to ion milling in SEMPA, or differences in the exact field sequence applied.

LTEM and SEMPA provide two complementary measurements of skyrmion structure - effectively, the limits of behavior at the surface, and the integrated behavior through the thickness. Compared quantitatively against micromagnetic simulation, and together with previous experimental work using neutron scattering to determine depth-dependent helicity, and theoretical studies calculating the depth-dependent

energetics, they provide a clear picture of the depth-dependent helicity and geometric properties of hybrid skyrmions in magnetic multilayer thin films.

3.4 Chapter Conclusion

In this chapter, we used a combination of surface-sensitive SEMPA and projective LTEM to experimentally determine the 3D structure of hybrid skyrmions in a well-studied multilayer thin film system, Fe/Gd multilayers. SEMPA measured all three components of the surface magnetization, while LTEM measured the integrated in-plane magnetic induction, together showing the Néel caps and a Bloch core, respectively. Because both techniques provide real-space images, we were able to quantify the helicity of the skyrmions. This was most important at the surface, where the amount by which the DWs twist toward Néel-type is indicative of the amount of additional stability granted by the hybrid structure. Real-space imaging also allowed for direct comparison to micromagnetic simulations, which provided a corroborating picture of the hybrid structure, including both the helicity and geometric size variation through the thickness. In general, the schema of combining surface-sensitive and projective real-space measurements can provide good understanding of the 3D structure of magnetic skyrmions, without the experimental difficulties that accompany tomographic techniques, or the interpretability complexity of reciprocal-space measurements.

One of the major advantages of multilayer thin films is their tunability. By tuning the number, thickness, and composition of layers, different magnetic behavior can be achieved. In the next chapter, we describe work performed to measure asymmetry introduced in Fe/Gd thin films by the inclusion of symmetry-breaking Pt and Ir layers in the stack.

CHAPTER IV

CHARACTERIZATION OF FIELD HISTORY DEPENDENT DOMAIN WALL CHIRALITY PREFERENCE

This work is not associated with a manuscript or publication. The project was conceived of and brought to my attention by Sergio Montoya. He fabricated all the samples used and developed the experimental procedure. I collected the LTEM data, developed the analysis technique, and performed the analysis.

4.1 Introduction

The promise of magnetic skyrmions as information bits in spintronic devices hinges on the ability to stabilize magnetic skyrmions in practical conditions, most notably at room temperature and in the absence of a large stabilizing magnetic field. This has led to a strong interest in multilayer thin films, which can host skyrmions in these conditions due to their tunability and the hybrid structure of their skyrmions [18]. In principal, these films require no symmetry-breaking mechanism to host skyrmions, instead relying on the balance of long-range and short-range energetics. As a result, left- and right-handed magnetic skyrmions can coexist in multilayer thin films in equal abundance.

This coexistance of chiralities presents the opportunity to tune the proportions of left- and right-handed skyrmions. Here I present Lorentz microscopy measurements that show how the inclusion of symmetry-breaking layers can create a chirality preference dependent on magnetic field history.

4.2 Measurements and Analysis

Fe/Gd/Fe/Pt/Ir multilayers were sputter deposited onto a silicon-nitride TEM window, with 5nm Ta seed and capping layers. The composition had a structure of 80 layers of [Fe (3.4 Å) / Gd (4.0 Å) / Fe (3.4 Å) / Pt (0.75 Å) / Ir (0.25

Å)]. Previous work performed simultaneous anisotropic magneto resistance (AMR) and Hall resistivity field-dependent measurements [44], and determined that this sample possesses a preferred chirality due to a topological Hall response. That work also performed initial Lorentz TEM measurements showing domain wall chirality preference following a positive saturation to negative saturation to slightly positive field cycle.

Here, I build on that work by performing Lorentz TEM measurements of the sample following four possible field sequences. In each, the field starts at either positive or negative perpendicular saturation, is then gradually removed until no field is being applied, and then a small, non-saturating field either above or below zero field is applied. This last small field is used to allow for differentiation between positive and negative domains based on domain width. Each of the four field sequences was repeated at both 140 K and 160 K.

Following the measurements, I used the domain wall tracing methods developed by Chess. *et al.* in [33] to trace a majority of domain wall pixels in each image. This method found greater than 80% of domain wall pixels, but each domain must be closed to assign it a positive or negative m_z. The remaining pixels were traced by hand in standard image processing software. At this point, the sign of m_z can be determined in two ways: first, by noting that the thinner domains should be anti-aligned with the applied field, and second, by following their growth as the field is decreased from saturation. Both methods were used, as the two matched.

The near-remanence magnetization configuration is labyrinthian domains, with a number of forks and Bloch points. Fig. 14 shows a representative raw Lorentz TEM image and the corresponding reconstructed magnetic induction. Magnetic induction was calculated using the single image transport of intensity equation

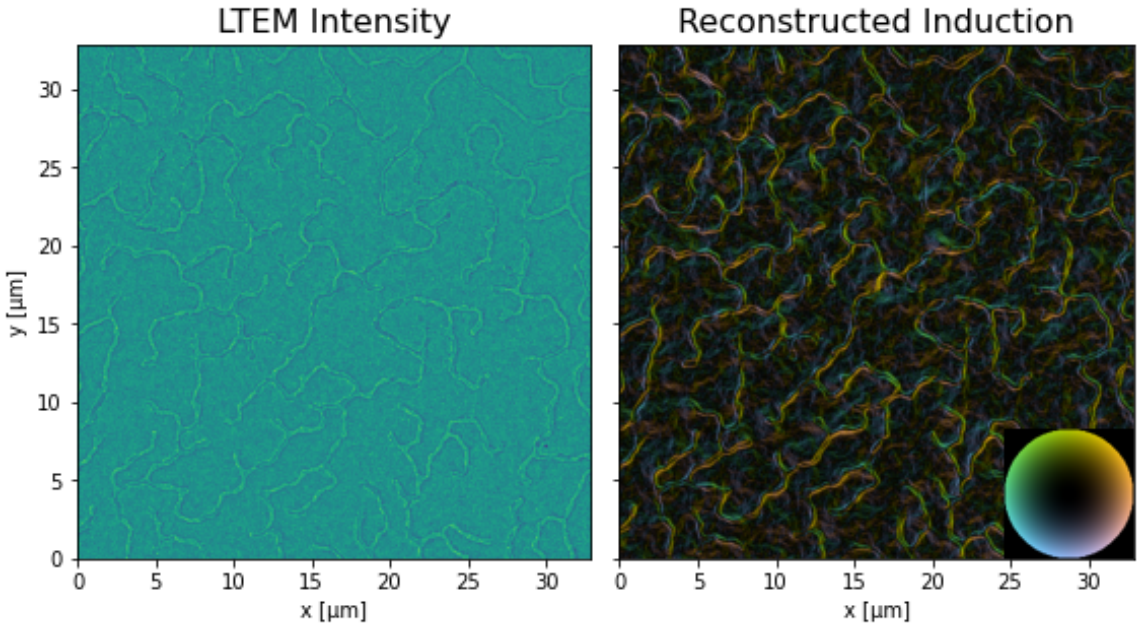

Figure 14. Representative Lorentz TEM image along with the reconstructed in-plane magnetic induction map. In the induction map, brightness represents the strength of in-plane magnetic induction and color represents its direction.

(SITIE) developed in [39]. Fig. 15 demonstrates how the chirality of a domain wall is defined as the angle between in-plane domain wall magnetization and the normal to the domain wall, using the same field of view as Fig. 14. The normal to the domain wall is taken as the gradient of m_z, such that it points from a domain where $m_z < 0$ to one where $m_z > 0$, resulting in $\alpha = \angle(\mathbf{m}_\perp, \nabla_\perp m_z)$. Fig. 16 shows all eight total chirality measurements taken, for two different temperatures and four field sequences.

Fig. 17 summarizes the findings. At both temperatures, the domain wall chirality is dependent on the saturating field prior to measurement. These results demonstrate a clear symmetry-breaking mechanism in these thin films with asymmetric layer stacking. However, while the high degree of chirality indicates a bulk DMI-like term in the energetics, the mechanism of this energy is not well understood. This work

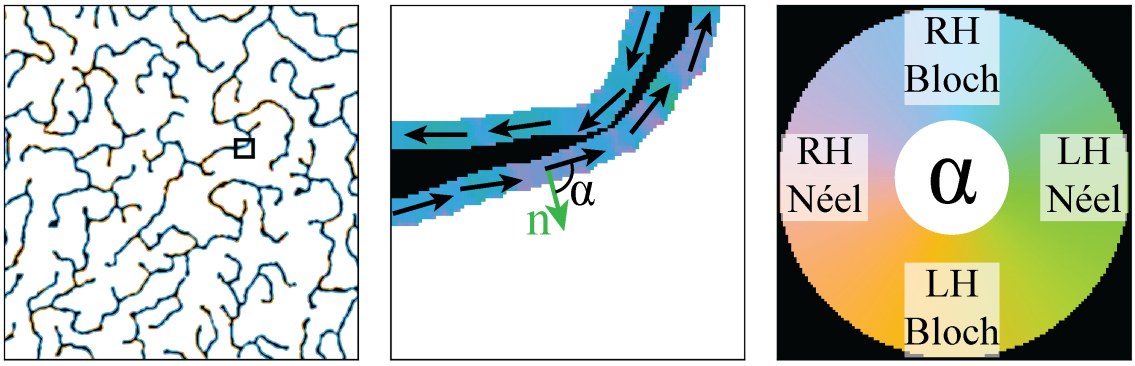

Figure 15. Chirality map and a schematic of the definition of domain wall chirality. The magnetic domains are colored by the sign of m_z, with black for $m_z < 0$ and white for $m_z > 0$. Domain walls are colored by their chirality.

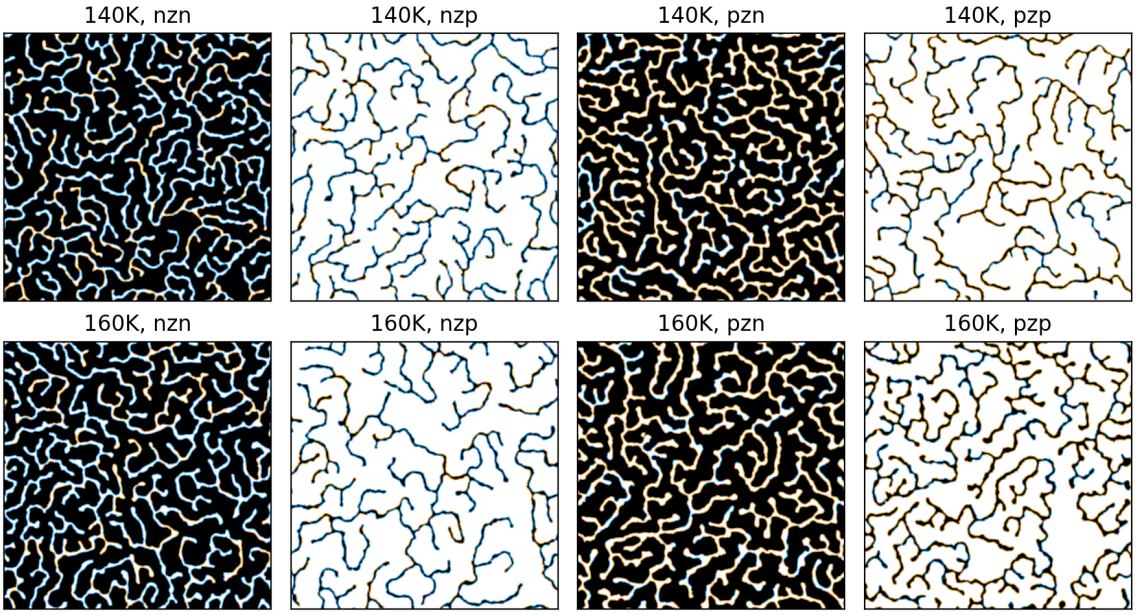

Figure 16. Chirality maps for both temperatures and all four field sequences. The field sequence is represented as "nzn" for negative saturation, to remanence, to slightly negative applied field, and so on.

requires further studies to fully understand the symmetry-breaking energetics, but already demonstrates the ability to control domain wall chirality reliably.

4.3 Chapter Conclusion

This chapter presented Lorentz TEM measurements and subsequent analysis of domain wall chirality. The results show that a Bloch domain wall chirality preference based on field history can be induced by asymmetric layer stacking. This asymmetry is not yet well understood, and requires further experimental and theoretical work. The dependence on field history, however, is a well-known characteristic of magnetic materials. By applying different sequences of magnetic field to the sample, a large variety of magnetic phases and novel spin textures can be created. In the next chapter, I examine one of these novel spin textures, the biskyrmion or skyrmion bound pair. Since the first report of its observation via LTEM, there has been debate over whether the texture is actually a skyrmion bound pair, as multiple structures can give similar signals in LTEM. To counter this difficulty, I track the novel texture's evolution from striped domain walls that break up into individual skyrmion bound pairs, taking advantage of the field history dependence in order to characterize an ambiguous LTEM signal.

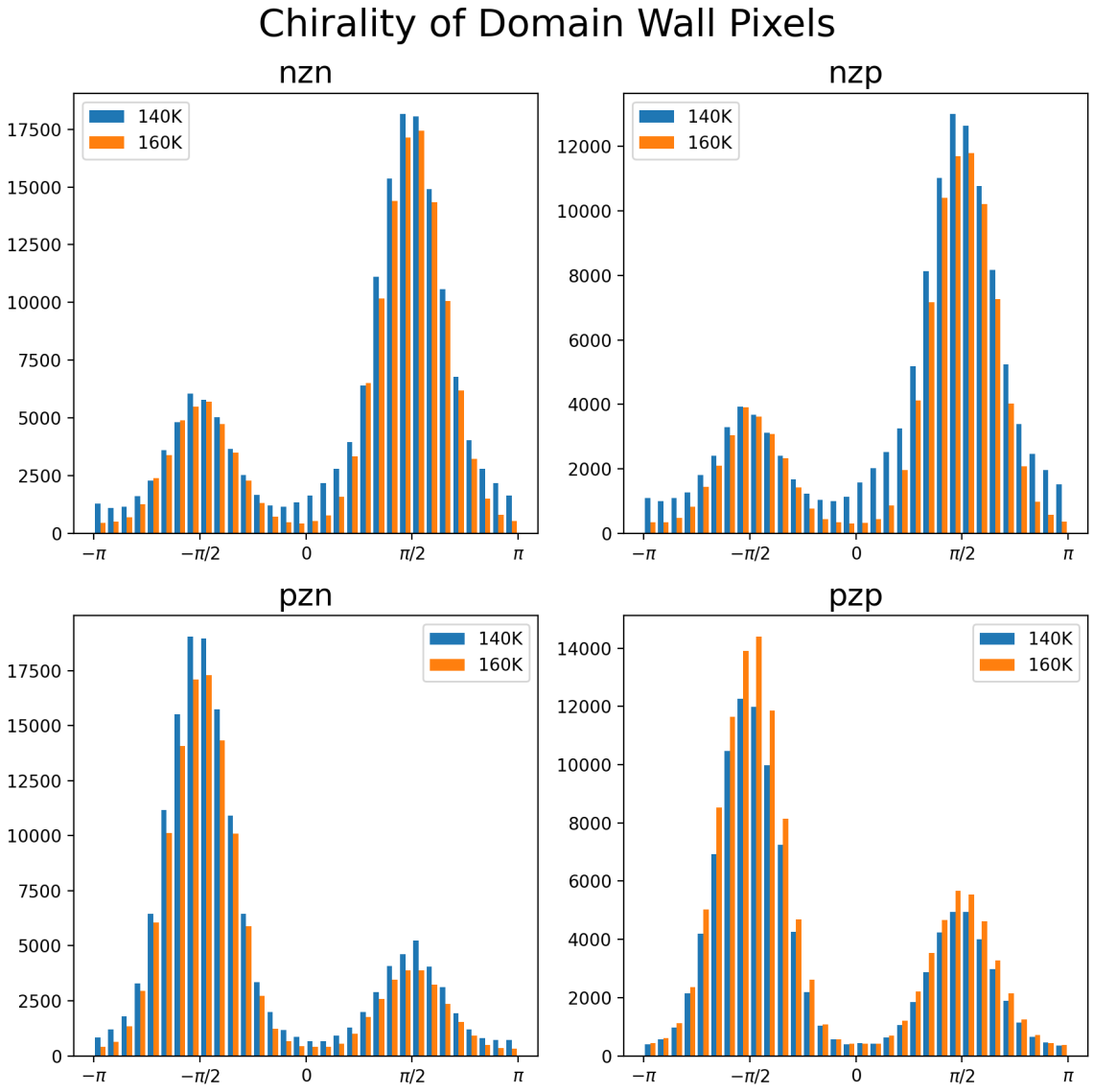

Figure 17. Histograms of the chirality of domain wall pixels. The field sequence used is represented in the title as "nzn" for negative saturation, to remanence, to slightly negative applied field, and so on.

CHAPTER V

TRACKING THE EVOLUTION OF BISKYRMION TEXTURES FROM DOMAIN WALL STRIPES

From Parker, W. S., Montoya, S. A., Fullerton, E. E., and McMorran, B. J. 2022. "Evolution of Novel Chiral Spin Textures in Fe/Gd Based Multilayer Thin Films." *Microscopy and Microanalysis* Volume 28, Issue S1, 1 August 2022, Pages 2336-2337. Sergio Montoya and Eric Fullerton study the novel textures in these materials and conceived of the overarching project. Sergio Montoya fabricated all samples used. Benjamin McMorran previously imaged the novel texture examined in this work. I conceived of the idea to study the novel texture by tracking its evolution. I collected all LTEM data and analyzed it. The following is not an exact replication of the published conference abstract, but is restructured to fit better within this dissertation.

5.1 Tracking the Evolution of Biskyrmion Textures from Domain Wall Stripes

Magnetic skyrmions are perhaps the primary motivation for studying magnetic thin films and other magnetic materials on the nanoscopic scale. Most proposals for spintronic devices using nanoscale magnetic textures involve magnetic skyrmions [19, 8, 45, 29]. However, there is a wide range of other spin textures possible in nanomagnetic systems, including in multilayer thin films [44]. In fact, multilayer thin films may be some of the most flexible nanomagnetic systems since their magnetic behavior is not tied to a crystalline structure or a single symmetry-breaking energetic term, such as DMI. As a result, based on the tuned parameters - number of layers, thickness of layers, and exact composition of the stack - as well as the field sequence applied to the thin film, several interesting spin textures may form. Whether these

spin textures are useful in spintronics or not, they often provide valuable insight into the energetics of the system [21].

Recently, a novel biskyrmion phase was reported in Fe/Gd multilayer thin films, consisting of bound pairs of skyrmions with opposite helicities [46]. They were observed using a combination of Lorentz TEM imaging and resonant X-ray techniques. However, Lorentz TEM is a projective technique, measuring only the in-plane magnetic field integrated through z, and resonant X-ray imaging is a projective technique which measures the projected out-of-plane magnetization, in reciprocal space. Neither provides a conclusive picture of the true structure, and subsequent work has suggested alternate interpretations of the data. In particular, Loudon *et al.* [47] note that a tilted trivial magnetic bubble may yield a qualitatively equivalent Lorentz TEM reconstruction, and Streubel *et al.* [48] note that a charge-2 skyrmion, with $N_{sk} = 2$, may do so as well. Fig. 18 shows the reconstructed induction found in experimental data. Fig. 19 shows how a similar induction map, also consisting of a pair of counter-rotating vortices, could be attributed to skyrmion bound pairs, $N_{sk} = 2$ skyrmions, or type-II bubbles. Trivial bubbles, or type-II bubbles, are common in these thin films, but generate significantly less interest due to a lack of topological protection. $N_{sk} = 2$ skyrmions have not yet been observed in these materials, but would be a very interesting development, as they have higher-order topological charge.

Here, rather than directly characterizing the structure of the novel texture, we use Lorentz TEM to track its evolution from the well-studied stripe domain phase. In Lorentz TEM, the objective lens is not needed and can therefore be used to apply a magnetic field sequence while simultaneously imaging the sample. To recreate the novel phase, we first apply an out-of-plane magnetic field, tilting the sample slightly so

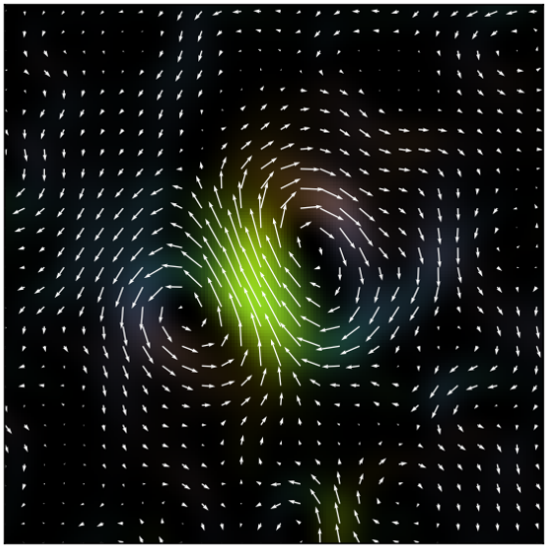

Figure 18. Magnetic induction of the novel texture. Reconstruction from Lorentz TEM images shows a pair of counter-rotating vortices.

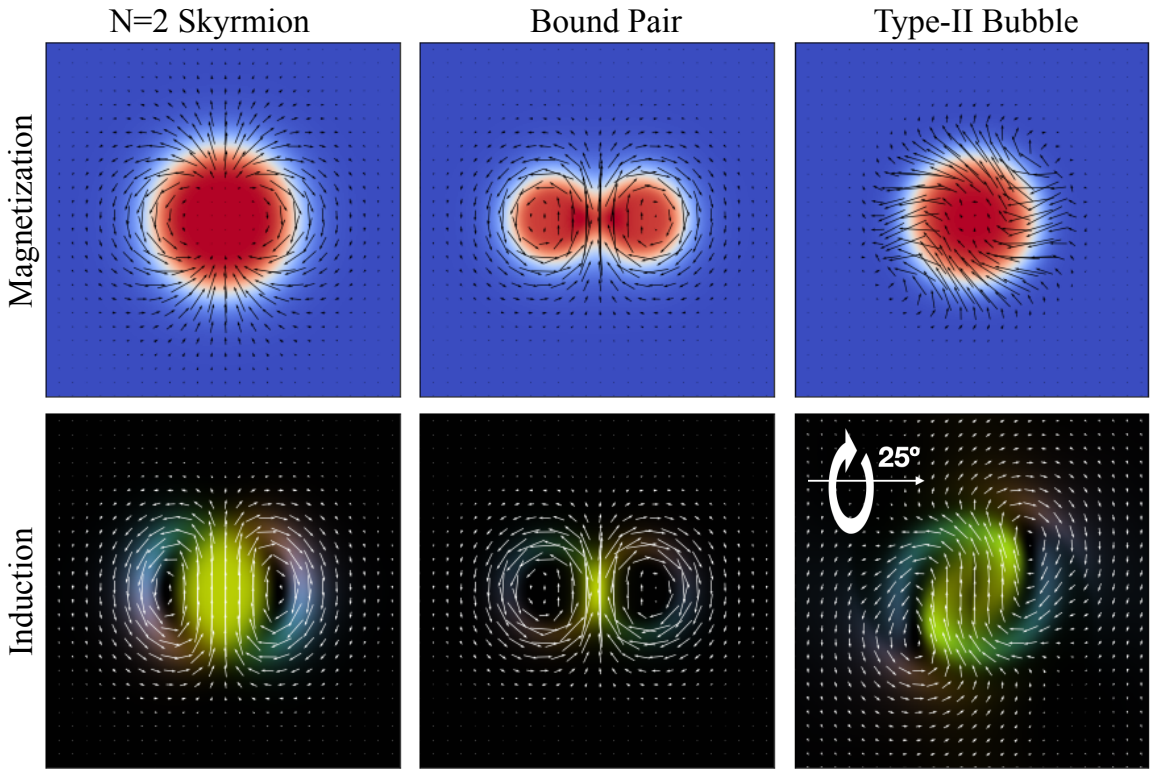

Figure 19. Comparison of the magnetic inductions for an $N_{sk} = 2$ skyrmion, a skyrmion bound pair, or biskyrmion, and a tilted type-II magnetic bubble.

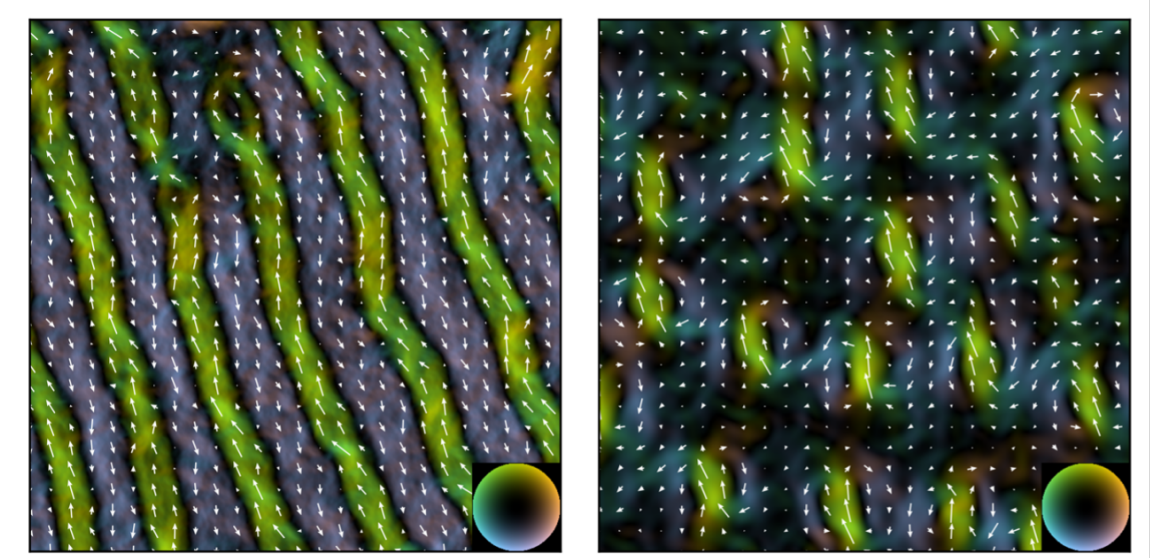

Figure 20. Evolution of biskyrmion textures from striped domain walls. The domain walls aligned with the external field form the cores of biskyrmions, while those anti-aligned form closure loops, resulting in a pair of counter-rotating magnetic vortices.

that there is a small field component in the plane of the thin film. This creates striped helical DWs, with adjacent DWs anti-parallel to each other, matching previous results [21]. As the field is increased, the DWs split along their length, and the DWs which are aligned to the external field remain quite strong. This progression is illustrated in Fig. 20. These form the center of the new, individual textures, while the adjacent DWs which are anti-aligned to the external field form closure loops. This supports the biskyrmion interpretation of Lorentz TEM data, suggesting that the center of the texture is actually a magnetic domain wall, and therefore that the full texture is a pair of counter-rotating vortices.

5.2 Chapter Conclusion

This chapter presents the results of a study which tracks the evolution of a novel spin texture from a well-understood spin texture. By tracking this evolution, we were able to better understand the structure of the resulting spin texture, and

showed that it corresponds to a pair of counter-rotating magnetic vortices. This supports the claim of Lee *et al.* [46], and is in agreement with the resonant X-ray data collected in that paper. The observation of this novel spin texture in Fe/Gd multilayers again demonstrates the versatility of this system. The new texture is not yet well understood, and three-dimensional imaging techniques will be required to learn the details of its formation and stability. Toward that end, the next chapter introduces STEM holography as a magnetic imaging technique. STEM holography is not a 3D technique, but it is a major improvement on the current TEM-based magnetic imaging techniques. Its ease of use, high resolution, and direct measurement of the phase make it a practical candidate for vector tomography.

CHAPTER VI

STEM HOLOGRAPHIC IMAGING OF MAGNETIC DOMAINS IN FE/GD MULTILAYER THIN FILMS

This chapter "STEM Holographic Imaging of Magnetic Domains in Fe/Gd Multilayer Thin Films" is a manuscript in preparation. The sample was prepared and studied previously by Sergio Montoya and Eric Fullerton. Fehmi Yasin and Xiuzhen Yu helped develop the experimental technique and the analysis process. Fehmi Yasin, Andrew Ducharme, and I collected the data. I wrote the majority of the manuscript, with substantial contribution from Andrew Ducharme.

6.1 Introduction

On the road to developing novel and useful magnetic materials, the ability to characterize magnetic textures is critical and it is currently lacking. A number of techniques, described in detail in Chapter 1.4, exist to image magnetic materials, but all are either projective or surface-sensitive, most are limited to one or two components of magnetization, and many are prohibitively difficult to implement, requiring either extremely customized microscope setups or synchrotron beamtime. As a result, much magnetic materials characterization is done via bulk measurements like hysteresis loops and transport measurements, leading to an unclear or unreliable understanding of the behavior. Here, we describe how a relatively new TEM technique, STEM holography (STEMH), can add to this field. It is still incomplete, being a projective measurement of the phase, but its ease-of-implementation and high quality make it a prime candidate for vector field tomography, which could provide a full 3D picture of magnetization.

6.2 STEM Holographic Imaging of Magnetic Domains in Fe/Gd Multilayer Thin Films

Electron interferometry, in principle, is identical to photon interferometry, but often lags decades, or even centuries, behind in implementation due to the lack of electron optical elements. The picometer-scale wavelength of the incident electron and its strong coupling to sample electromagnetic fields make the reward for solving this technical challenge, atomic-resolution interferometry, very enticing. Without mirrors or beamsplitters, the first realization of an electron interferometer used three copper crystals to divide the amplitude of the electron beam [49]. However, the historically predominant technique of this type is electron holography [50, 51], where an electrostatically charged wire, or electron biprism, splits a parallel electron beam in a TEM post-specimen and creates an interference pattern at the detector. In the realm of magnetic imaging, electron holography, using bespoke TEMs, has measured skyrmions [37], magnetic bubbles, stripe domains [52], and even the magnetic field of individual lattice planes [53].

Despite its success, biprism electron holography has been hampered by a few experimental drawbacks. The electron beam must be spatially coherent at roughly the length scale of the biprism wire width, requiring more expensive field-emission electron sources [50, 54]. As an activated biprism splits the electron beam around itself, an installed but inactive biprism blocks the electron beam and prevents standard usage of the microscope. In use, the two resulting beams are not optically ideal. They exhibit Fresnel diffraction and tend to be asymmetric, which introduces imaging artifacts. These Fresnel effects can be eliminated with the addition of one or more biprisms throughout the microscope column and the attendant tradeoffs therein.

An alternative realization of electron holography has recently been developed which instead uses a nanofabricated diffraction grating to split the amplitude of the electron beam [55, 56]. Made with focused ion beam (FIB) instruments on silicon nitride membrane windows, gratings have spatial periods on the order of hundreds of nanometers. The small period reduces the coherence requirements on the electron source compared to biprism setups, and the off-the-shelf SiN windows can be inserted into standard condenser aperture slots of commercially available TEMs. These gratings are often in a saved aperture location unused by normal users and are not in the beam path, so the interferometer is layered atop the extensive existing capabilities of commercial instruments without serious customization, and is imperceptible to the normal user. However, as nanofabricated elements, gratings sacrifice the tunable path separation of biprisms. The interference patterns also must be captured on 4DSTEM detectors, which, while becoming less expensive, still have not achieved universal adoption in TEM laboratories.

Here, we use a nanofabricated diffraction grating to create an electron interferometer with the microscope in low-mag STEM mode, in which the objective lens is disabled, to acquire a real-space image of magnetic domains. Disabling the objective lens is necessary for magnetic specimens, as its roughly 1T magnetic field would otherwise overwhelm the magnetic behavior of the specimen, but it sacrifices the sub-nanometer resolution otherwise available in commercial TEMs. Without the objective lens, the beam separation (and hence the field of view) increases from the order of tens of nanometers to microns. The interferometer is rastered across the sample, at each point measuring the Aharonov-Bohm phase shift imparted by the magnetic field of the sample. From this phase shift, the magnetic induction is calculated directly.

STEMH is analogous to other TEM-based magnetic imaging techniques such as DPC and LTEM, but with several distinct advantages. It directly measures the Aharonov-Bohm phase of the sample probe relative to the vacuum probe, while DPC measures the gradient of the phase and LTEM forms contrast proportional to the 2D Laplacian of the phase, both of which introduce noise. It requires no defocus, as LTEM does, and so its resolution is fundamentally limited only by the microscope's abilities. It has exceptional phase sensitivity, so imaging thin and low-contrast samples is possible. Perhaps most importantly, it is a non-intrusive modification to standard STEM imaging. This makes it easy to implement, and it means its quality will continue to improve at the rapid pace of general STEM techniques.

The interferometer setup, shown in Fig. 21, was achieved in the TEAM I modified FEI Titan 80-300 keV microscope at the National Center for Electron Microscopy (NCEM), which was used for its Gatan K3 IS direct electron detector. The aberration corrector was not used. The diffraction grating is milled into a SiN membrane of 30 nm thickness using an FEI Helios Dual Beam FIB - 600i. The membrane underside is coated with Ti and Pt for adhesion and charge alleviation respectively. It is placed in the second condenser (C2) aperture of the microscope so that the electron beam diffracts through it to form multiple probes at the sample plane. By tailoring the depth of the grooves, a majority of the electron beam's amplitude is directed to the +1, 0, and -1 diffraction orders. Adjacent probes are separated by 2.4 µm in the sample plane.

Using this technique, we imaged a Fe/Gd magnetic multilayer thin film, a material which is of substantial interest due to its ability to host magnetic skyrmions within a tunable range of temperatures and applied fields. In our case, 120 layers of alternating Fe and Gd were sputter deposited onto a perforated SiN membrane, with

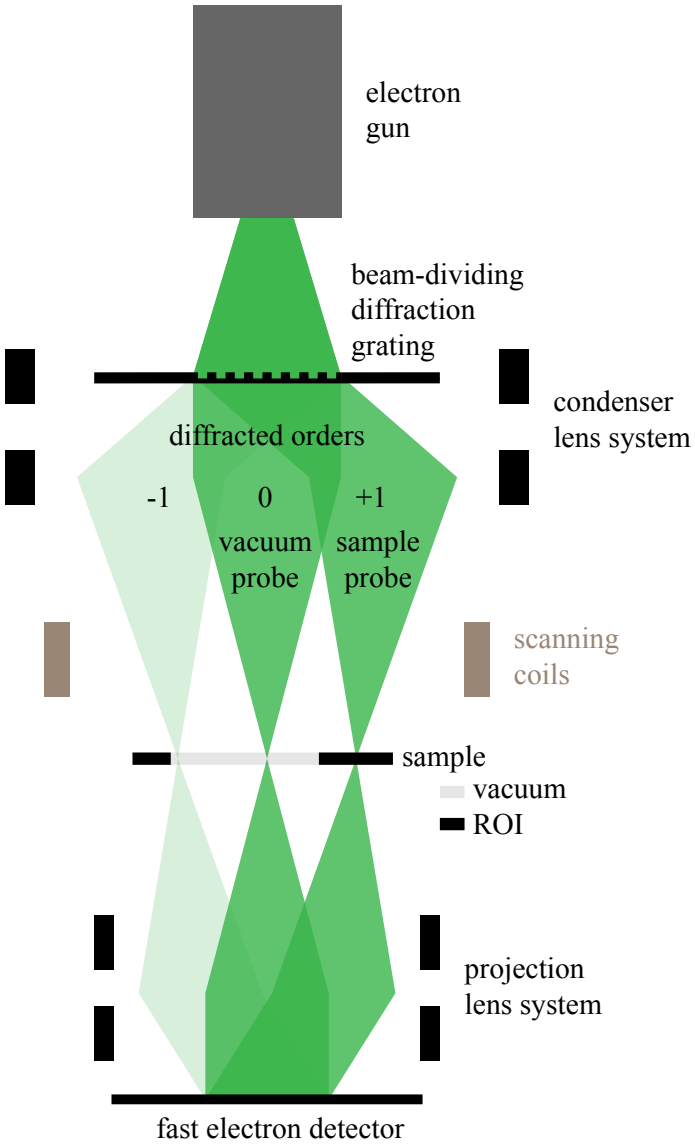

Figure 21. Schematic of the STEMH setup. A beam-dividing diffraction grating is placed into the C2 (probe-forming) aperture of the microscope, splitting the beam into multiple diffraction orders. Its depth profile is designed so that the majority of beam intensity is split between the 0 and +1 orders, which pass through the sample and vacuum, respectively. The projection system then recombines the probes onto the detector, forming an image of the grating modulated by the relative phase acquired by the sample probe as it passes through the sample.

both seed and capping layers of Pt to prevent oxidation. The sample has an out-of-plane easy axis, with stripe or labyrinthian magnetic domains at remanence, separated by domain walls with a strong Bloch component. Depending on the orientation of neighboring domain walls and the sequence of magnetic field applied prior to imaging, the magnetic domain widths are between 100-200 nm. The SiN substrate is perforated by a grid of 30 µm diameter holes, leaving ample room for the vacuum region probes to pass through.

The probe passing through the sample acquires a phase shift

$$\begin{aligned}\phi(\mathbf{r}_\perp) &= C_E \int_L V(\mathbf{r}_\perp, z)dz - \frac{\pi}{\Phi_0}\int_L \mathbf{A}(\mathbf{r}_\perp, z)\cdot d\mathbf{r} \\ &= \phi_e + \phi_m\end{aligned} \tag{6.1}$$

due to the Aharonov-Bohm effect, with L the electron's path, $\mathbf{r}_\perp$ the coordinates transverse to the optical axis, C_E the interaction constant and Φ_0 the magnetic flux quantum. ϕ_e and ϕ_m are the contributions from electric and magnetic fields, respectively. Typically the two components are isolated by flipping the sample, which will flip the sign of the magnetic component but not the electric. However, for a uniform sample such as ours, the electric component adds only a constant phase related to the mean inner potential to the probe, and can therefore be ignored.

After the sample, the microscope's post-specimen optics recombine the probes onto the 4DSTEM detector in the reciprocal plane of the sample, which records an interference pattern for each point in the STEM scan. Taking a fast Fourier transform (FFT) of the interference pattern allows us to isolate the relative phases of pairs of probes. By selecting the first peak, we can ascertain the relative phases of probes separated by one order; in our case, this gives the relative phase shift between the 0 and +1 orders, one of which passed through the sample and one of which passed through vacuum, which we call the sample and vacuum probes respectively.

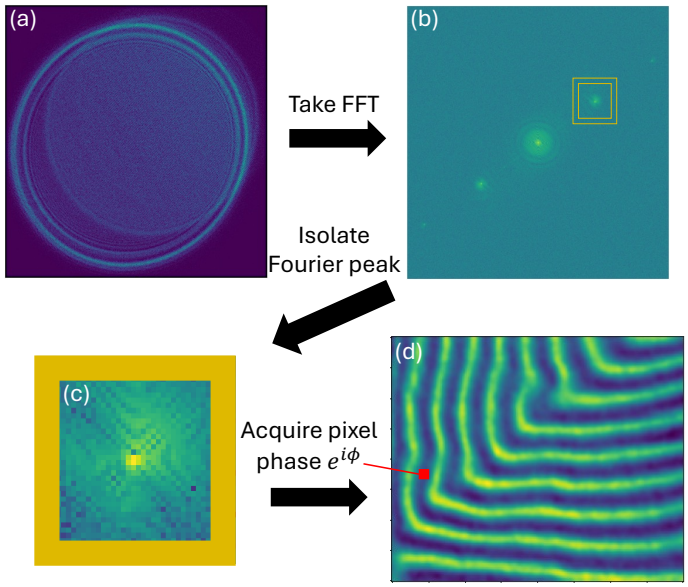

Figure 22. Reconstruction algorithm for each interference pattern captured during the 4DSTEM scan. The interference pattern (a), an individual frame in the 4DSTEM raster, is fast Fourier transformed to produce (b). The interference of the order 0 and +1 probes due to the material phase is contained at peaks closest to the center. We isolate this peak in (c) and acquire the phase of the complex-valued peak. This phase is the value plotted in a particular pixel in (d).

Again, since the sample is uniform we assume all variations in phase are due to the magnetic field of the sample, and the reconstructed phase represents simply ϕ_m. The reconstruction process is diagrammed in Fig. 22.

From the magnetic phase map ϕ_m, the in-plane magnetic induction $\mathbf{B}(\mathbf{r}_\perp)$ can be calculated using the relation

$$\nabla_\perp \phi_m(\mathbf{r}_\perp) = \frac{-e\tau}{\hbar}\mathbf{B}(\mathbf{r}_\perp) \times \hat{\mathbf{z}} \tag{6.2}$$

with $\hat{\mathbf{z}}$ the vector parallel to the electron beam's propagation. Note that from the above relation, the component of magnetic field parallel to the electron beam's trajectory does not contribute to signal. This means that only in-plane magnetization is visible – in our case, these are the domain walls rather than the domains themselves. This is a general limitation of magnetic imaging using fast electrons; X-

ray magnetic imaging techniques such as X-ray magnetic circular dichroism (XMCD) complement electron microscopy by being sensitive only to the parallel component of magnetization. In both areas, tomography may be used to gain a full picture of magnetization, at the cost of experimental complexity. In addition, the signal is integrated in z, and stray fields can therefore have a non-negligible effect, making a direct link between magnetic induction and magnetization difficult to establish.

Fig. 23 shows (a) the acquired phase map and (b) the reconstructed magnetic induction. It shows striped magnetic domains with a bend. In these materials, remanence configurations are typically somewhere between straight stripe domains and labyrinthian domains, and depend on the exact field sequence applied prior to imaging. In this case, we set the microscope's objective lens to 10% strength, immersing the sample in a roughly 330mT applied field, which should saturate it, before decreasing the applied field to remanence. Effects due to the edge of the vacuum region of the sample may also contribute to the domains' sharp change of direction.

We quantified domain wall spacing for comparison with Lorentz TEM data by measuring the average distance between domain walls. Fig. 23 (c) and (d) show horizontal and vertical line scans of the in-plane magnetization $|B_\perp|^2$, respectively. The distance between neighboring domain walls was measured to be 98 ± 21.67 nm for the horizontal line scan and 100 ± 27.57 nm for the vertical line scan. Fig. 24 shows a Lorentz TEM image of an identical sample, again with (a) the acquired phase, (b) the reconstructed induction, and (c) a vertical line scan of in-plane magnetization shown. Domain wall spacing was measured in the same way, albeit with only a vertical line scan, giving an average spacing of 99 ± 15.67 nm between domain walls. Note that the LTEM image shows a mixture of chiral and achiral domains (that is,

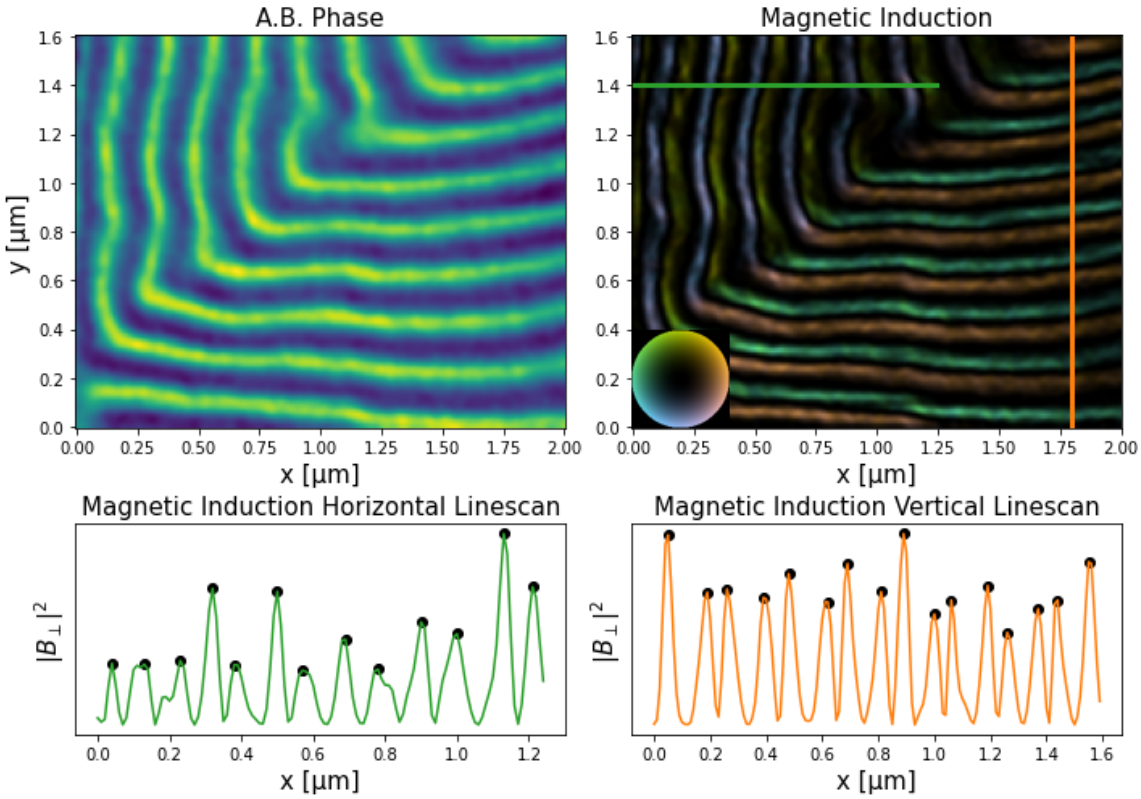

Figure 23. (a) The measured phase, (b) the reconstructed magnetic induction, and (c) and (d) horizontal and vertical line scans of the in-plane magnetic induction, respectively, as measured by STEM holography in a field-free condition.

some adjacent domain walls are aligned and some are anti-aligned) while the STEMH image shows purely chiral domains. Both of these are common remanence states for Fe/Gd multilayer thin films.

This experiment has extended the capabilities of STEM holography by applying the technique to a magnetic sample with the TEM's objective lens disabled. That extension shows the flexibility of STEMH, as despite the drastic decrease in quality that disabling the objective lens has on the probe, phase was still retrievable at a high enough resolution to resolve magnetic domains of a scientifically interesting sample. Moreover, applying STEMH to magnetic imaging is an exciting development, as it provides real-space magnetic phase data comparable to Lorentz TEM but without

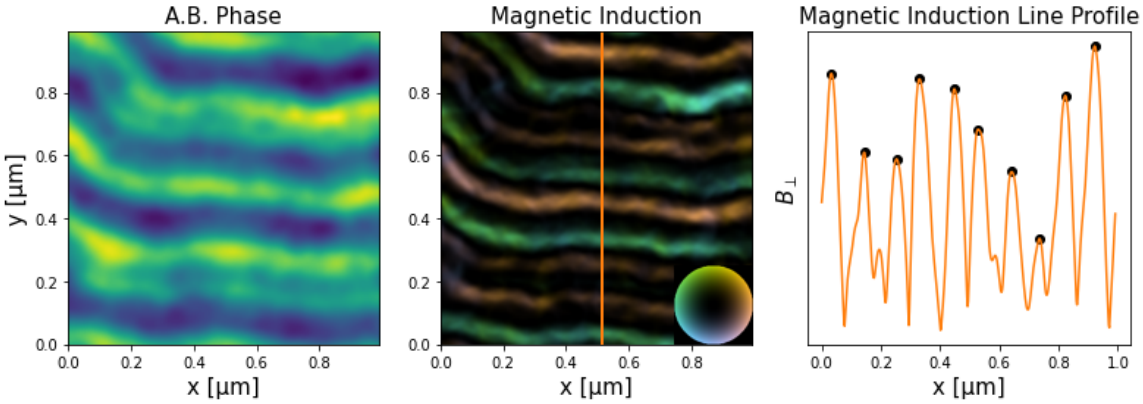

Figure 24. (a) The measured phase, (b) the reconstructed magnetic induction, and (c) a vertical line scan of the in-plane magnetic induction, as measured by Lorentz TEM.

the need to defocus the beam or a dedicated Lorentz lens. Since the technique can be achieved by simply inserting an aperture into existing aperture slots in a commercial STEM instrument, this technique is both accessible and yields high quality results, and as STEM instruments continue improve, magnetic STEMH will improve concurrently.

6.3 Chapter Conclusion

In this chapter we applied STEM holography to a magnetic sample. This is a technique the McMorran group has pioneered, using nanofabricated diffraction gratings to make the technique practical and high-quality. To apply it to a magnetic sample, the objective lens was turned off, and the sample was deposited on a substrate with a vacuum region. Removing the objective lens decreases the maximum resolution, but by directly measuring the phase through interferometry, this technique avoids the need to defocus as in Lorentz TEM, and removes the noise that comes from measuring only differential phase rather than absolute. In addition, microscopes are being developed whose objective lens does not immerse the sample in a magnetic field, and they could be used to implement this technique at the maximum resolution

of electron microscopy. In the next chapter, we describe a proposal for another novel imaging technique using vortex electron beams to measure chiral dichroism in the TEM. This dichroism measurement could measure chiral nanoparticles, chiral molecules, or the z-component of magnetization directly - something most TEM magnetic imaging techniques cannot.

CHAPTER VII

A PROPOSAL FOR MEASURING CHIRAL DICHROISM IN THE ELECTRON MICROSCOPE

7.1 Introduction

In Chapter VI, we introduced a novel method for imaging magnetic materials in an electron microscope, magnetic STEMH. At its core, magnetic STEMH is another phase retrieval method. It relies on the fact that a fast electron passing through a magnetic field, or a magnetic vector potential, acquires a phase shift on its way through. In terms of the magnetic field, this phase shift depends only on the component transverse to the electron's path, so for a thin, flat sample, magnetic STEMH and all other projective phase retrieval techniques access the in-plane component of magnetic field. They do not access the magnetization directly, and they do not access the out-of-plane component of magnetic field.

We have seen in Chapter III how the spin angular momentum (SAM) of secondary electrons ejected from the surface can tell us about the magnetization of a material. However, the electron has other degrees of freedom. In particular, McMorran *et al.* [57] specialize in creating vortex electron beams, which have quantized orbital angular momentum (OAM) in relation to the optical axis. Fast electrons can exchange this OAM when interacting with a sample, and the resulting asymmetric scattering into OAM modes creates a dichroism signal [58, 59, 60, 61, 62]. This is analogous to circular dichroism in photon optics, in which left- and right-handed circularly polarized light is asymmetrically absorbed.

In the case of electron OAM, the exchange typically accompanies inelastic interactions, so rather than measuring absorption spectra like we would for photons, we can measure energy-loss spectra. This type of interaction is relatively general for

electrons, and by filtering on a certain energy-loss we can isolate specific dichroic interactions. Many commercial transmission electron microscopes have electron energy loss spectrometers (EELS) which can filter transmitted electrons by energy loss. However, filtering electrons by OAM gain/loss is a non-trivial problem. One solution involves using custom electron optics post-specimen to spatially separate electrons by OAM component, but this setup is costly and difficult to align, as well as requiring multiple apertures post-specimen, which are typically not available on conventional TEMs [63]. In this chapter, I describe a proposed method for spatially isolating electrons which have gained or lost $1\hbar$ of OAM interacting with the sample, using a single nanofabricated diffraction grating post-specimen, so that they can then be fed into conventional EELS systems.

7.2 Dichroic Interactions

There are two types of dichroic interactions which would be highly interesting to study with electrons. The first is electron energy-loss magnetic chiral dichroism (EMCD), in which the fast electron exchanges both energy and OAM to excite an atomic transition. The interaction is dichroic when the atom prefers to either gain or lose OAM in a certain transition. This happens, for example, in the L-edge of transition metals, where the unpaired valence electrons cause a spin imbalance, resulting in spin-polarized atomic transitions. Since the valence spin polarization couples to atomic orbital angular momentum, the transition also becomes OAM-polarized. As this spin imbalance, and subsequent spin-orbit coupling, is also what we call magnetism, accessing this chiral dichroism would directly measure the magnetization of the atom addressed. In particular, since the OAM of a fast electron is with respect to the optical axis, the dichroic signal would access the out-of-plane

magnetization of the sample, rather than the in-plane magnetic field seen by phase retrieval techniques.

This interaction is analogous to the established technique of X-ray magnetic circular dichroism (XMCD) [64]. In fact, in atomic interactions the OAM of fast electrons plays an equivalent role to the SAM of photons [62]. However, EMCD has distinct advantages over XMCD. Fast electron imaging can be achieved in commercially available TEMs, while XMCD requires synchrotrons for most magnetic materials. At the same time, the resolution available to fast electrons far exceeds that of X-rays as atomic resolution in the TEM is relatively commonplace.

The second type of dichroism is structural. Molecules and nanostructures can have geometric chirality, which can strongly affect their behavior. In particular, many biomolecules are chiral, and can react in biochemical reactions very differently based on their chirality [65]. This makes determination of molecular chirality an extremely useful ability. The structural chirality of nanostructures and molecules manifests itself as a dichroic plasmon response [58]. Fast electrons passing a nanostructure inelastically excite coherent electron oscillations in the nanostructure, known as plasmons. This inelastic interaction is accompanied by OAM exchange, which should be asymmetric when the nanostructure is chiral, as a given plasmon mode in a chiral nanostructure has OAM.

7.3 Measuring OAM Exchange with a Post-Selecting Forked Grating

For the proposed measurement scheme, we want to compare the energy-loss spectra of the $\pm 1\hbar$ OAM components of an electron beam that has interacted with the sample. To do so, we make use of the spatial amplitude distribution of electrons with non-zero OAM. Electrons with non-zero OAM have a characteristic donut shape, with zero intensity along the beam axis. Conversely, electrons with zero OAM fill in

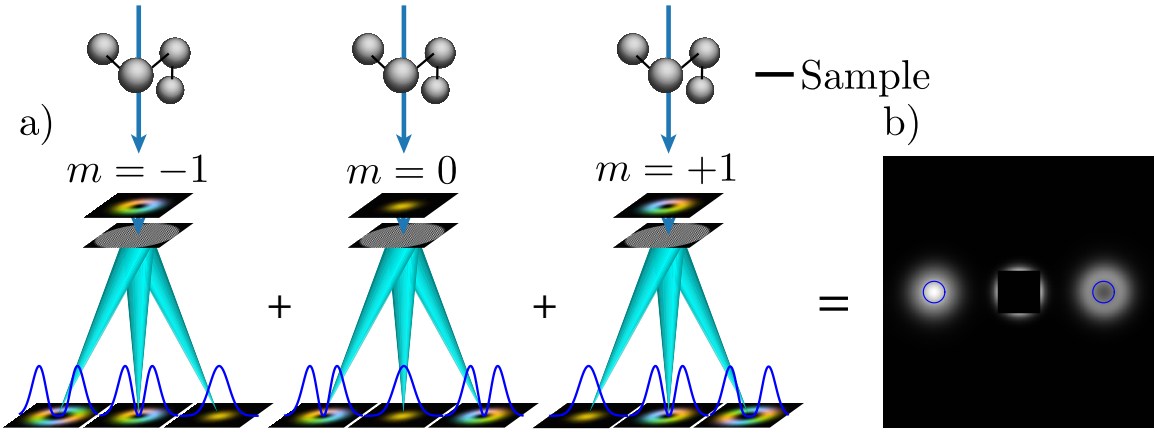

Figure 25. Schematic of the dichroism measurement scheme. (a) An electron scatters off a sample into a beam composed of three components, with $-1\hbar$, $0\hbar$, and $1\hbar$ of OAM from left to right, before passing through a forked diffraction grating which adds $\pm 1\hbar$ in the ± 1 diffracted orders. (b) Assuming the electron beam was most likely to leave the sample with $+1\hbar$ of OAM, the center of the -1 diffracted order will then be stronger than the center of the $+1$ diffracted order.

along the beam axis. We can make use of this by placing a forked diffraction grating after the interaction with the sample. The zeroth diffracted order remains unchanged, but the ± 1 diffracted orders gain $\pm 1\hbar$ of OAM. The result is that any intensity along the optical axis of the $+1(-1)$ diffracted order comes from the $-1\hbar(+1\hbar)$ component of the scattered OAM beam (Fig. 25). To then measure energy loss spectra, we can isolate the center of the diffracted beams using an aperture before sending each through the EELS device.

7.4 Chapter Conclusion

In this chapter, a scheme was proposed to measure dichroic interactions in a commercial TEM. This would allow for both structural chirality measurements and direct measurements of the z-component of magnetization, with all the benefits that come with commercial TEMs. The measurement scheme would also be minimally intrusive and cost-effective, and could be implemented in most standard TEMs which have EELS systems.

CHAPTER VIII

CONCLUSION AND FUTURE DIRECTIONS

We showed how the additional 3D structure present in hybrid skyrmions creates novel, knotted topological structure. This manifests as a non-zero but fractional 3D topological charge, the Hopf index, and we showed how the underlying mathematical structure of the Hopf index, the Hopf fibration, can be used to construct hybrid skyrmions. We combined surface-sensitive SEMPA and projective LTEM magnetic imaging techniques to gain a real-space understanding of the hybrid structure. In both regards, results were compared against micromagnetic simulations for a complete picture. As a result, there is now both a theoretical framework for understanding the topological nature of hybrid skyrmions, and a method for their real-space characterization, with direct quantitative links between the two.

Having developed a framework for understanding and characterizing the structure of hybrid skyrmions, the clear path forward is to apply it to the questions hindering skyrmions' use in real world applications. In particular, these should be applied to generating current driven motion at low current densities, developing smaller and more stable skyrmions in a range of materials, and understanding more exotic spin textures. It is becoming clear that the 3D structure of skyrmions has an important role to play in their stability and behavior, so both the novel characterization techniques and the theoretical framework developed here will be useful in future studies.

We applied a novel imaging technique, STEM holography with nanofabricated diffraction gratings, to magnetic samples. The multitude of advantages this technique has over existing magnetic imaging techniques opens the door for tomographic magnetic imaging for a complete 3D picture of magnetic samples, atomic resolution

magnetic imaging for ferrimagnetic and nanoscopic textures, and high-sensitivity phase imaging for ultra-thin magnetic materials. In general, STEM holography is a form of 4D-STEM, and will benefit from all of the exceptional advances being made in 4D-STEM currently.

The need to characterize magnetic spin textures is critical to the development of future spin-based logic and memory devices. So too is the need to understand and predict their behavior, dynamics, and stability. The fractional Hopfion framework provides groundwork for the latter, while the combination of SEMPA with projective imaging provides tools for the former. As the 3D structure of magnetic materials gains importance, this type of multimodal imaging is invaluable. Finally, using STEM holography as the projective imaging technique in that modality provides opportunity for drastic improvements, including full 3D characterization through vector field tomography, and has the potential to create a quantized step forward in the way we develop and understand magnetic materials.

APPENDIX A

APPENDIX TO HYBRID SKYRMIONS IN MAGNETIC MULTILAYER THIN FILMS ARE HALF-INTEGER HOPFIONS

A.1 Detailed Construction From Hopf Fibration

The Hopf fibration is a set of curves on the 3-sphere $\mathbb{S}^3$ defined by the fibers of the Hopf map - the fibers of a function being all the elements of its domain that map to the same point. For example, the set $\{-1, 1\}$ can be considered one fiber of the function $f(x) = x^2$, as $f(-1) = f(1) = 1$. The Hopf map is the many-to-one continuous function from the 3-sphere to the ordinary 2-sphere $h : \mathbb{S}^3 \to \mathbb{S}^2$ defined by

$$h(x_1, y_1, x_2, y_2) = \begin{pmatrix} 2(x_1x_2 + y_1y_2) \\ 2(y_1x_2 - x_1y_2) \\ x_1^2 + y_1^2 - x_2^2 - y_2^2 \end{pmatrix}, \tag{A.1}$$

whose fibers form circles on the 3-sphere. It can be directly verified that if two points (x_1, y_1, x_2, y_2) and (x_1', y_1', x_2', y_2') map to the same point under the Hopf map - that is, $h(x_1, y_1, x_2, y_2) = h(x_1', y_1', x_2', y_2')$ - then the two points can be related as follows

$$\begin{pmatrix} x_1' \\ y_1' \\ x_2' \\ y_2' \end{pmatrix} = \begin{pmatrix} \cos t & -\sin t & 0 & 0 \\ \sin t & \cos t & 0 & 0 \\ 0 & 0 & \cos t & -\sin t \\ 0 & 0 & \sin t & \cos t \end{pmatrix} \begin{pmatrix} x_1 \\ y_1 \\ x_2 \\ y_2 \end{pmatrix}, \tag{A.2}$$

for any $t \in [0, 2\pi)$, defining a circle in $\mathbb{S}^3$. We can use this relation to write the Hopf fiber passing through an initial point $(x_1, y_1, x_2, y_2) \in \mathbb{S}^3$ as a parametric curve

$$\mathbf{s}(t) = \begin{pmatrix} x_1 \cos t - y_1 \sin t \\ x_1 \sin t + y_1 \cos t \\ x_2 \cos t - y_2 \sin t \\ x_2 \sin t + y_2 \cos t \end{pmatrix}. \tag{A.3}$$

We can relate this fiber to 3D space $\mathbb{R}^3$ via the stereographic projection, given by

$$\begin{pmatrix} S_1 \\ S_2 \\ S_3 \end{pmatrix} = \frac{1}{1 - s_4} \begin{pmatrix} s_1 \\ s_2 \\ s_3 \end{pmatrix}. \tag{A.4}$$

Applying this to Eq. (A.3) gives an equation for the Hopf fiber in $\mathbb{R}^3$

$$\mathbf{S}(t) = \frac{1}{1 - x_2 \sin t - y_2 \cos t} \times \begin{pmatrix} x_1 \cos t - y_1 \sin t \\ x_1 \sin t + y_1 \cos t \\ x_2 \cos t - y_2 \sin t \end{pmatrix}. \tag{A.5}$$

However, this is expressed in terms of an initial point $(x_1, y_1, x_2, y_2) \in \mathbb{S}^3$. We can relate this initial point to the initial point in $\mathbb{R}^3$ via the inverse stereographic projection, given by

$$\begin{pmatrix} x_1 \\ y_1 \\ x_2 \\ y_2 \end{pmatrix} = \frac{1}{1 + R^2} \begin{pmatrix} 2x \\ 2y \\ 2z \\ R^2 - 1 \end{pmatrix} \tag{A.6}$$

where $R^2 = x^2 + y^2 + z^2$. Substitution of Eq. (A.6) into Eq. (A.5) gives the result Eq. (2.1), which is a parametrization of the Hopf fiber which passes through an initial point (x, y, z).

A.2 Numerical calculation of the Hopf index

To numerically calculate the Hopf index, it is necessary to evaluate Eq. (2.8). $\mathbf{F}$ contains only spatial derivatives of $\mathbf{m}$, and is therefore straightforward to calculate numerically. $\mathbf{A}$ is defined implicitly via $\nabla \times \mathbf{A} = \mathbf{F}$ and is therefore less trivial. To calculate $\mathbf{A}$, we choose the Coulomb gauge $\nabla \cdot \mathbf{A} = 0$, so that we can use the identity

$$\nabla \times (\nabla \times \mathbf{A}) = \nabla(\nabla \cdot \mathbf{A}) - \nabla^2 \mathbf{A} \tag{A.7}$$

which, substituting the implicit defintion of $\mathbf{A}$ on the LHS and the Coulomb gauge condition on the RHS, reduces to

$$\nabla \times \mathbf{F} = -\nabla^2 \mathbf{A}. \tag{A.8}$$

This is Poisson's equation, and it can be numerically solved with a variety of existing techniques - for example, by using Fourier transforms to replace differentiation with multiplication.

APPENDIX B

DEVELOPMENT AND PACKAGING OF PYTHON CODE FOR LTEM ANALYSIS, SIMULATION, AND VISUALIZATION.

In the course of my studies, I developed an extensive code base for the analysis, simulation, and presentation of Lorentz TEM data. As this code base grew, I built it into a Python package, and extended its capabilities to be a useful tool kit for all things magnetics and Lorentz TEM. Most notably, I made it open-source and publicly available on PyPI, the Python Package Index, so that it is installable via `pip`, the most common method of Python package installation. The documentation (available at `https://mcmorranlab.github.io/ltempy/index.html`) is extensive and is hosted on the McMorran Lab's GitHub. This appendix is intended to serve as an introduction to my package for all future LTEM and magnetics users, within the McMorran Lab and without. It is also an appeal to all physicists who rely on Python to develop their code base into a distributable package, as the benefits are immense.

B.1 ltempy

My Python package, `ltempy`, consists of several modules. It began as a simple implementation of the single image transport of intensity equation (SITIE) developed by Jordan Chess [39], but came to include first basic image processing tools, and then an implementation of simulations based on Mansuripur *et al.* [41]. Now, it includes SITIE reconstruction, a suite of plotting routines specific to magnetic imaging, a suite of 2D image processing utilities, and a module dedicated to simulating magnetic phase, magnetic field, magnetic vector potential, and electron propagation through the TEM. It is distributed through PyPI, meaning installation is simple: `python -m pip install ltempy`. No scientifically novel techniques developed by myself are represented in this package, although SITIE and the magnetic simulations

are both relatively scientifically novel. Instead, I include this appendix because the act of packaging and formalizing my own code base has been immeasurably useful throughout my studies, and I hope that `ltempy` can be useful to others.

REFERENCES CITED

[1] Recording Telephones. *Nature*, 62(1607):371–373, August 1900.

[2] Arman Shehabi, Sarah Smith, Dale Sartor, Richard Brown, Magnus Herrlin, Jonathan Koomey, Eric Masanet, Nathaniel Horner, Inês Azevedo, and William Lintner. United States Data Center Energy Usage Report. Technical report, June 2016.

[3] Powering Intelligence: Analyzing Artificial Intelligence and Data Center Energy Consumption. White Paper 000000003002028905, Electric Power Research Institute.

[4] David Brock. Software as Hardware: Apollo's Rope Memory.

[5] Y. Tarui, Y. Hayashi, and K. Nagai. Electrically reprogrammable nonvolatile semiconductor memory. *IEEE J. Solid-State Circuits*, 7(5):369–375, October 1972.

[6] Donald K. Rose, Peter J. Silverman, and Hudson A. Washburn. Technology and Manufacturing of High-Density Magnetic-Bubble Memories. In *VLSI Electronics Microstructure Science*, volume 4, pages 147–181. Elsevier, 1982.

[7] Stuart S. P. Parkin, Masamitsu Hayashi, and Luc Thomas. Magnetic Domain-Wall Racetrack Memory. *Science*, 320(5873):190–194, April 2008.

[8] Albert Fert, Vincent Cros, and João Sampaio. Skyrmions on the track. *Nature Nanotech*, 8(3):152–156, March 2013.

[9] T.H.R. Skyrme. A non-linear field theory. *Proc. R. Soc. Lond. A*, 260(1300):127–138, February 1961.

[10] T.H.R. Skyrme. A unified field theory of mesons and baryons. *Nuclear Physics*, 31:556–569, March 1962.

[11] S. Mühlbauer, B. Binz, F. Jonietz, C. Pfleiderer, A. Rosch, A. Neubauer, R. Georgii, and P. Böni. Skyrmion Lattice in a Chiral Magnet. *Science*, 323(5916):915–919, February 2009.

[12] X. Z. Yu, Y. Onose, N. Kanazawa, J. H. Park, J. H. Han, Y. Matsui, N. Nagaosa, and Y. Tokura. Real-space observation of a two-dimensional skyrmion crystal. *Nature*, 465(7300):901–904, June 2010.

[13] X.Z. Yu, N. Kanazawa, W.Z. Zhang, T. Nagai, T. Hara, K. Kimoto, Y. Matsui, Y. Onose, and Y. Tokura. Skyrmion flow near room temperature in an ultralow current density. *Nat Commun*, 3(1):988, August 2012.

[14] Arne Vansteenkiste, Jonathan Leliaert, Mykola Dvornik, Mathias Helsen, Felipe Garcia-Sanchez, and Bartel Van Waeyenberge. The design and verification of MuMax3. *AIP Advances*, 4(10):107133, October 2014.

[15] J. H. C. Whitehead. An Expression of Hopf's Invariant as an Integral. *Proc. Natl. Acad. Sci. U.S.A.*, 33(5):117–123, May 1947.

[16] X. Z. Yu, N. Kanazawa, Y. Onose, K. Kimoto, W. Z. Zhang, S. Ishiwata, Y. Matsui, and Y. Tokura. Near room-temperature formation of a skyrmion crystal in thin-films of the helimagnet FeGe. *Nature Mater*, 10(2):106–109, February 2011.

[17] Naoto Nagaosa and Yoshinori Tokura. Topological properties and dynamics of magnetic skyrmions. *Nature Nanotech*, 8(12):899–911, December 2013.

[18] Ryan D. Desautels, Lisa DeBeer-Schmitt, Sergio A. Montoya, Julie A. Borchers, Soong-Geun Je, Nan Tang, Mi-Young Im, Michael R. Fitzsimmons, Eric E. Fullerton, and Dustin A. Gilbert. Realization of ordered magnetic skyrmions in thin films at ambient conditions. *Phys. Rev. Materials*, 3(10):104406, October 2019.

[19] Wanjun Jiang, Gong Chen, Kai Liu, Jiadong Zang, Suzanne G.E. te Velthuis, and Axel Hoffmann. Skyrmions in magnetic multilayers. *Physics Reports*, 704:1–49, August 2017.

[20] S. A. Montoya, S. Couture, J. J. Chess, J. C. T. Lee, N. Kent, M.-Y. Im, S. D. Kevan, P. Fischer, B. J. McMorran, S. Roy, V. Lomakin, and E. E. Fullerton. Resonant properties of dipole skyrmions in amorphous Fe/Gd multilayers. *Phys. Rev. B*, 95(22):224405, June 2017.

[21] S. A. Montoya, S. Couture, J. J. Chess, J. C. T. Lee, N. Kent, D. Henze, S. K. Sinha, M.-Y. Im, S. D. Kevan, P. Fischer, B. J. McMorran, V. Lomakin, S. Roy, and E. E. Fullerton. Tailoring magnetic energies to form dipole skyrmions and skyrmion lattices. *Phys. Rev. B*, 95(2):024415, January 2017.

[22] Ivan Lemesh and Geoffrey S. D. Beach. Twisted domain walls and skyrmions in perpendicularly magnetized multilayers. *Phys. Rev. B*, 98(10):104402, September 2018.

[23] W. L. N. C. Liyanage, Nan Tang, Lizabeth Quigley, Julie A. Borchers, Alexander J. Grutter, Brian B. Maranville, Sunil K. Sinha, Nicolas Reyren, Sergio A. Montoya, Eric E. Fullerton, Lisa DeBeer-Schmitt, and Dustin A. Gilbert. Three-dimensional structure of hybrid magnetic skyrmions determined by neutron scattering. *Phys. Rev. B*, 107(18):184412, May 2023.

[24] Alice T. Greenberg. *The Application of Interferometric Electron Microscopy for Nanomagnetic Imaging*. PhD thesis, University of Oregon, Eugene, Oregon, USA, October 2020.

[25] Jing Xia, Xichao Zhang, Xiaoxi Liu, Yan Zhou, and Motohiko Ezawa. Qubits based on merons in magnetic nanodisks. *Commun Mater*, 3(1):88, November 2022.

[26] F. Tejo, R. Hernández Heredero, O. Chubykalo-Fesenko, and K. Y. Guslienko. The Bloch point 3D topological charge induced by the magnetostatic interaction. *Sci Rep*, 11(1):21714, November 2021.

[27] P. Coullet, L. Gil, and F. Rocca. Optical vortices. *Optics Communications*, 73(5):403–408, November 1989.

[28] Börge Göbel, Alexander Mook, Jürgen Henk, Ingrid Mertig, and Oleg A. Tretiakov. Magnetic bimerons as skyrmion analogues in in-plane magnets. *Phys. Rev. B*, 99(6):060407, February 2019.

[29] Noah Kent, Neal Reynolds, David Raftrey, Ian T. G. Campbell, Selven Virasawmy, Scott Dhuey, Rajesh V. Chopdekar, Aurelio Hierro-Rodriguez, Andrea Sorrentino, Eva Pereiro, Salvador Ferrer, Frances Hellman, Paul Sutcliffe, and Peter Fischer. Creation and observation of Hopfions in magnetic multilayer systems. *Nat Commun*, 12(1):1562, March 2021.

[30] L. Faddeev and Antti J. Niemi. Stable knot-like structures in classical field theory. *Nature*, 387(6628):58–61, May 1997.

[31] Egor Babaev, Ludvig D. Faddeev, and Antti J. Niemi. Hidden symmetry and knot solitons in a charged two-condensate Bose system. *Phys. Rev. B*, 65(10):100512, February 2002.

[32] A. M. Kamchatnov. Topological soliton in magnetohydrodynamics. 2004.

[33] Jordan J. Chess, Sergio A. Montoya, Eric E. Fullerton, and Benjamin J. McMorran. Determination of domain wall chirality using in situ Lorentz transmission electron microscopy. *AIP Advances*, 7(5):056807, February 2017.

[34] Jens Gladikowski and Meik Hellmund. Static solitons with nonzero Hopf number. *Phys. Rev. D*, 56(8):5194–5199, October 1997.

[35] William Legrand, Jean-Yves Chauleau, Davide Maccariello, Nicolas Reyren, Sophie Collin, Karim Bouzehouane, Nicolas Jaouen, Vincent Cros, and Albert Fert. Hybrid chiral domain walls and skyrmions in magnetic multilayers. *Sci. Adv.*, 4(7):eaat0415, July 2018.

[36] Nan Tang, Jung-Wei Liao, Siu-Tat Chui, Timothy Ziman, Alexander J. Grutter, Kai Liu, Chih-Huang Lai, Brian J. Kirby, and Dustin A. Gilbert. Controlling magnetic configuration in soft–hard bilayers probed by polarized neutron reflectometry. *APL Materials*, 10(1):011107, January 2022.

[37] Hyun Soon Park, Xiuzhen Yu, Shinji Aizawa, Toshiaki Tanigaki, Tetsuya Akashi, Yoshio Takahashi, Tsuyoshi Matsuda, Naoya Kanazawa, Yoshinori Onose, Daisuke Shindo, Akira Tonomura, and Yoshinori Tokura. Observation of the magnetic flux and three-dimensional structure of skyrmion lattices by electron holography. *Nature Nanotech*, 9(5):337–342, May 2014.

[38] John Unguris. 6. Scanning electron microscopy with polarization analysis (SEMPA) and its applications. In *Experimental Methods in the Physical Sciences*, volume 36, pages 167–XVI. Elsevier, 2001.

[39] Jordan J. Chess, Sergio A. Montoya, Tyler R. Harvey, Colin Ophus, Simon Couture, Vitaliy Lomakin, Eric E. Fullerton, and Benjamin J. McMorran. Streamlined approach to mapping the magnetic induction of skyrmionic materials. *Ultramicroscopy*, 177:78–83, June 2017.

[40] D. L. Abraham and H. Hopster. Magnetic probing depth in spin-polarized secondary electron spectroscopy. *Phys Rev Lett*, 58(13):1352–1354, March 1987.

[41] M. Mansuripur. Computation of electron diffraction patterns in Lorentz electron microscopy of thin magnetic films. *Journal of Applied Physics*, 69(4):2455–2464, February 1991.

[42] C. Steger. An unbiased detector of curvilinear structures. *IEEE Trans. Pattern Anal. Machine Intell.*, 20(2):113–125, Feb./1998.

[43] Thorsten Wagner, Mark Hiner, and Xraynaud. Thorstenwagner/ij-ridgedetection: Ridge Detection 1.4.0. Zenodo, August 2017.

[44] Jordan J. Chess. *Mapping Topological Magnetization and Magnetic Skyrmions*. PhD thesis, University of Oregon, University of Oregon, Eugene, Oregon, 2017.

[45] Yan Zhou. Magnetic skyrmions: Intriguing physics and new spintronic device concepts. *National Science Review*, 6(2):210–212, March 2019.

[46] J. C. T. Lee, J. J. Chess, S. A. Montoya, X. Shi, N. Tamura, S. K. Mishra, P. Fischer, B. J. McMorran, S. K. Sinha, E. E. Fullerton, S. D. Kevan, and S. Roy. Synthesizing skyrmion bound pairs in Fe-Gd thin films. *Applied Physics Letters*, 109(2):022402, July 2016.

[47] James C. Loudon, Alison C. Twitchett-Harrison, David Cortés-Ortuño, Max T. Birch, Luke A. Turnbull, Aleš Štefančič, Feodor Y. Ogrin, Erick O. Burgos-Parra, Nicholas Bukin, Angus Laurenson, Horia Popescu, Marijan Beg, Ondrej Hovorka, Hans Fangohr, Paul A. Midgley, Geetha Balakrishnan, and Peter D. Hatton. Do Images of Biskyrmions Show Type-II Bubbles? *Advanced Materials*, 31(16):1806598, 2019.

[48] Robert Streubel, D. Simca Bouma, Frank Bruni, Xiaoqian Chen, Peter Ercius, Jim Ciston, Alpha T. N'Diaye, Sujoy Roy, Steve D. Kevan, Peter Fischer, and Frances Hellman. Chiral Spin Textures in Amorphous Iron–Germanium Thick Films. *Adv. Mater.*, 33(8):2004830, February 2021.

[49] L. Marton, J. Arol Simpson, and J. A. Suddeth. Electron Beam Interferometer. *Phys. Rev.*, 90(3):490–491, May 1953.

[50] G F Missiroli, G Pozzi, and U Valdre. Electron interferometry and interference electron microscopy. *J. Phys. E: Sci. Instrum.*, 14(6):649–671, June 1981.

[51] Ken Harada. Interference and interferometry in electron holography. *Microscopy*, 70(1):3–16, February 2021.

[52] Ken Harada, Hiroshi Nakajima, Keiko Shimada, Shigeo Mori, and Yoshio Takahashi. Electron holography for observing magnetic bubbles and stripe-shaped domains in magnetic fields. *Micron*, 160:103306, September 2022.

[53] Toshiaki Tanigaki, Tetsuya Akashi, Takaho Yoshida, Ken Harada, Kazuo Ishizuka, Masahiko Ichimura, Kazutaka Mitsuishi, Yasuhide Tomioka, Xiuzhen Yu, Daisuke Shindo, Yoshinori Tokura, Yasukazu Murakami, and Hiroyuki Shinada. Electron holography observation of individual ferrimagnetic lattice planes. *Nature*, 631(8021):521–525, July 2024.

[54] Q. Ru. Incoherent electron holography. *Journal of Applied Physics*, 77(4):1421–1426, February 1995.

[55] Fehmi S. Yasin, Tyler R. Harvey, Jordan J. Chess, Jordan S. Pierce, Colin Ophus, Peter Ercius, and Benjamin J. McMorran. Probing Light Atoms at Subnanometer Resolution: Realization of Scanning Transmission Electron Microscope Holography. *Nano Lett.*, 18(11):7118–7123, November 2018.

[56] Tyler R. Harvey, Fehmi S. Yasin, Jordan J. Chess, Jordan S. Pierce, Roberto M. S. dos Reis, Vasfi Burak Özdöl, Peter Ercius, Jim Ciston, Wenchun Feng, Nicholas A. Kotov, Benjamin J. McMorran, and Colin Ophus. Interpretable and Efficient Interferometric Contrast in Scanning Transmission Electron Microscopy with a Diffraction-Grating Beam Splitter. *Phys. Rev. Applied*, 10(6):061001, December 2018.

[57] Benjamin J. McMorran, Amit Agrawal, Ian M. Anderson, Andrew A. Herzing, Henri J. Lezec, Jabez J. McClelland, and John Unguris. Electron Vortex Beams with High Quanta of Orbital Angular Momentum. *Science*, 331(6014):192–195, January 2011.

[58] A. Asenjo-Garcia and F. J. García de Abajo. Dichroism in the interaction between vortex electron beams, plasmons, and molecules. *Phys. Rev. Lett.*, 113(6):066102, August 2014.

[59] C. Hébert, P. Schattschneider, S. Rubino, P. Novak, J. Rusz, and M. Stöger-Pollach. Magnetic circular dichroism in electron energy loss spectrometry. *Ultramicroscopy*, 108(3):277–284, 2008.

[60] T. Schachinger, S. Löffler, A. Steiger-Thirsfeld, M. Stöger-Pollach, S. Schneider, D. Pohl, B. Rellinghaus, and P. Schattschneider. EMCD with an electron vortex filter: Limitations and possibilities. *Ultramicroscopy*, 179:15–23, 2017.

[61] Tyler R. Harvey, Jordan S. Pierce, Jordan J. Chess, and Benjamin J. McMorran. Demonstration of electron helical dichroism as a local probe of chirality. *arXiv:1507.01810*, July 2015.

[62] Ruben Van Boxem, Bart Partoens, and Jo Verbeeck. Inelastic electron-vortex-beam scattering. *Physical Review A*, 91(3), March 2015.

[63] Amir H. Tavabi, Paolo Rosi, Enzo Rotunno, Alberto Roncaglia, Luca Belsito, Stefano Frabboni, Giulio Pozzi, Gian Carlo Gazzadi, Peng-Han Lu, Robert Nijland, Moumita Ghosh, Peter Tiemeijer, Ebrahim Karimi, Rafal E. Dunin-Borkowski, and Vincenzo Grillo. Experimental Demonstration of an Electrostatic Orbital Angular Momentum Sorter for Electron Beams. *Phys. Rev. Lett.*, 126(9):094802, March 2021.

[64] J. Stöhr. X-ray magnetic circular dichroism spectroscopy of transition metal thin films. *Journal of Electron Spectroscopy and Related Phenomena*, 75:253–272, December 1995.

[65] Uwe Meierhenrich. *Amino Acids and the Asymmetry of Life: Caught in the Act of Formation*. Advances in Astrobiology and Biogeophysics. Springer, Berlin, 2008.